Silicon (2021) 13:1619–1640
https://doi.org/10.1007/s12633-020-00538-7

ORIGINAL PAPER

Multi-Response Optimization of ECDM Parameters for Silica (Quartz) Using Grey Relational Analysis

Vivekshel Rajput[1] · Sanjay Singh Pundir[1] · Mudimallana Goud[1] · Narendra Mohan Suri[1]

Received: 30 October 2019 / Accepted: 1 June 2020 / Published online: 20 June 2020

Abstract
Electrochemical discharge machining (ECDM) has successfully demonstrated the micro-machining of pioneering engineering materials, regardless of their properties such as glass, quartz, silicon nitride ceramics, composites, etc. Yet numerous intrinsic challenges are there that should be addressed during the micro-hole drilling process with ECDM such as low material removal rate (MRR), high area of the heat-affected zone (HAZ), high hole tapering (HT), high radial overcut (ROC) and circularity error (CE). However, the determination of the input parameters' optimum level for multi-response parameters is still a strenuous work. This present study investigates the machining performance of the ECDM process during the machining of silica (Quartz) through establishing the optimum combination of the level of the parameters for multi-response parameters. MRR, HAZ, HT, ROC, and CE were picked as response parameters. Experiments were performed in consonance with Taguchi's L9 orthogonal array and response measurements were analyzed through Grey Relational Analysis (GRA) to identify the optimum levels of input process parameters for their combined fusion i.e. maximum MRR, minimum HAZ, minimum HT, minimum ROC, and minimum CE. Results exhibited that electrolyte concentration (wt.%) is the utmost governing input parameter followed by applied voltage (V) and inter-electrode gap ((IEG), mm) for controlling the multi-response parameters simultaneously. GRA optimized parameters were determined as 35 V, 15 wt.%, and 25 mm with 68.34% contribution only from the electrolyte concentration. Based on experimental investigation, micro-holes were successfully drilled on Silica (quartz) material with the success of the utilized method to assess the machining performance of the electrochemical discharge machining process.

Keywords Material removal rate · Micro-holes · Electrochemical discharge machining · Overcut · Tapering · Grey relational analysis

1 Introduction

With the rapid increment in the demand of micro-products in modern industries such as aerospace, bio-medical, nuclear, optics, electronics, and communication, etc., there has been progress in the advancement of micro-machining processes. It has prompted the miniaturization of engineering materials such as glass, ceramics, quartz, silicon nitride ceramics, etc. Quartz (Silica or silicon dioxide) is identified as one of the prominent materials to satisfy the demands in prominent engineering applications such as apertures for bilayer fluidic devices [1], micro-sensors for pressure sensing [2], light trapping in solar cells [3], micro-balancing [4]. Quartz exhibits excellent chemical and physical properties such as hardness, brittleness, low thermal expansion coefficient, and resistance to chemicals [5]. The refractive nature of quartz is considered as one of the pinnacle properties which makes it ideal for industrial use. Inferable from the brittle nature of quartz material, it becomes impossible to machine this material using the traditional method of machining. Although many non-conventional techniques such as ultrasonic machining (USM), laser beam machining (LBM), abrasive jet machining (AJM) can be utilized for machining quartz materials yet some specific intrinsic limitations are associated with machining processes like high thermal damage to the surface, high investment cost, low rate of material removal [6–8].

Electrochemical discharge machining (ECDM) is acknowledged as the hybridized machining process which is prevalently utilized for machining quartz material and other electrically non-conducting materials [9–12]. The electrical

✉ Vivekshel Rajput
sheelrajput03@gmail.com

[1] Production and Industrial Engineering Department, Punjab Engineering College, Chandigarh 160012, India

discharge releases immense thermal heating which removes the work material inferable to its melting and vaporization. The chemical action results in additional fine fewer material removals and aids in achieving the superior surface finish. Thus, the material removal in ECDM is the combined result of local Joule heating due to thermal heating [10–13] and chemical dissolution in the electrolyte [14–16]. ECDM was effectively used to machine Glass [14, 15], Ceramics [13], Quartz [17, 18], Silicon wafers [19], Polymer-based composites [20], Super-alloys [21] and Metal matrix composite [22]. ECDM is likewise perceived by other names such as Spark assisted chemical engraving (SACE) [15], Electrochemical spark machining (ECSM) [20]; Electro-chemical anode machining (ECAM) [23]. Khairy et al. [24] successfully inferred that the removal rate of work material and its dimensional correctness are more preferable in the ECDM process when compared to individual electrochemical machining (ECM) and electric discharge machining (EDM) process. The process was first demonstrated by Kurafuji in 1968 [25] in which they successfully drilled glass material by utilizing the electrical discharges. They emphasized the possibilities of drilling micro-holes in glass materials.

Till now, many empirical and analytical studies have been accounted for in the ECDM process to enhance its industrial and commercial utilization. Basak and Ghosh [10] successfully demonstrated the spark mechanism in the ECDM process and emphasized that the phenomenon of sparking is similar to ON/Off action of an electric switch. Wuthrich et al. [14–16] made monumental contributions in the field of ECDM and vigorously stated that the formation of gas film at the tool electrode vicinity is the essential parameter for determining machining efficiency and its repeatability. They likewise accentuated that spark at tool-electrolyte interface produces only once when a gas film is formed and the critical value of voltage is achieved. Sundaram et al. [26] studied the phenomena of gas film formation and its quality by analyzing the quality of hole diameter and HAZ. It was discovered that the application of pulse voltage produces a smaller hole diameter and HAZ. Tang et al. [27] emphasized that gas film is very crucial for spark generation and for continuing the machining process in ECDM. They studied the effect of current signals on the gas film evolution process at the tool vicinity. It was observed that the current pulses with peak values larger than 1A during the discharge stage were the electrolysis currents. When a current pulse occurred, a gas bubble was simultaneously produced to repair the defective gas film.

Many authors revealed that electrolyte type and its concentration played a crucial role in determining the viscosity of electrolyte. It increments with the increase in electrolyte concentration and results in the smoother machined surface because of enhanced chemical etching action [28, 29]. Numerous researchers have demonstrated the utilization of different electrolytes like sodium hydroxide (NaOH), potassium hydroxide (KOH), sodium chloride (NaCl) and sodium nitrate ($NaNO_3$). NaOH and KOH tend to produce high MRR since the presence of hydroxide (OH) radicals and results in smoother surface finish. NaCl and $NaNO_3$ electrolytes form sludge in the electrolyte and contaminate it which lowers the MRR [30]. Further, chemical etching action can be enhanced by mixing two electrolytes such as (NaOH +KOH) which enhances the rate of material removal and surface quality [31]. Chen et al. [32] utilized the self-developed auxiliary nozzle as assistance to the ECDM process that provided a coaxial jet which enabled the tool electrode to be submerged inside the electrolyte at a low level. Because of that, effective circulation of electrolyte and a concentrated spark was achieved. As a result, HAZ (1.732 mm^2) was reduced significantly while the surface finish was improved at the entrance and exit of the hole.

Saranya et al. [33] fabricated micro-holes with a ROC of 0.1640 mm at a constant feed rate of 0.8 μm/s using a spherical tool electrode. They performed a micro-hole fabrication process for 10 min that may result in larger overcut due to prolonged exposure of the sparks over the hole entrance. Tang et al. [34] utilized an insulated helical tool with gravity feed to scrutinize the micro-hole characteristics. The helical tool facilitates in the fresh replenishment of the electrolyte at higher depths that could result in less tapering. Many authors reported that the insulated tool electrode improves the microstructure quality of the machined surface by reducing the sparks from the tool side walls [35, 36]. They also discovered that the tool rotation improves the spark consistencies and causes less HAZ. Goud et al. [37] utilized a constant feed rate of range 3–5 mm/min for machining and discovered that low feed rate exposes the work material top surface to sparks for a more extended period. It increases the interaction time and subsequent high overcut is obtained. Jain et al. [38] applied a constant feed rate of 0.339 mm/min for evaluating the effect of polarity. They revealed that reverse polarity causes high overcut and high tool wear.

Various researchers reported that ECDM performance can be further enhanced by aiding it with other methods such as providing rotation and ultrasonic vibrations to tool electrode [39, 40], abrasive coated tools [41, 42], powder mixed ECDM [43], travelling wire ECDM [18, 29, 44], the assistance of magnetic field [5, 45] and utilizing different shapes of tools [46]. Rajput et al. [47] highlighted the future areas for enhancing the ECDM performance and represented the critical analysis on the effect of process parameters on different work materials.

Optimization of input process parameters is a vital process and serves a key to identify the range of most influential input process parameters which control the machining performance in the ECDM process. Taguchi's techniques are considered as a vigorous tool for enhancing the quality of the response measurements [49, 50]. Signal to Noise (S/N) ratios are commonly

used for optimizing the single response characteristic for all input process parameters. Subsequently, the optimum parameter is chosen with a higher S/N ratio for all the response characteristics irrespective of different objectives i.e., one has to maximize (*ex: MRR*) while others have to minimize (*ex: HT*). Despite this, the S/N ratio does not account for the simultaneous effect of different objectives for multi-response optimization. For this reason, the issue of multi-response optimization turns out to be more strenuous when compared to solitary optimization as it relates to better response characteristics. In order to subdue this complication, grey relational analysis, which was first demonstrated by Deng in 1982 [51], is widely used to improve the quality of the multi-response characteristics. GRA technique is reported to be a robust technique for successfully optimizing the multi-response parameters during micro-machining operation with ECDM [37, 52–54].

1.1 Problem Formulation

Based on the literature, it has been observed that ECDM exhibits diverse applications in the discipline of Micro-Electro-Mechanical Systems (MEMS), electronic industry, biomedical equipment, micro-fluidic, micro-accelerometers, micro-pumps, etc. [1, 2, 55]. A substantial number of publications demonstrated the ECDM's machining possibilities on difficult to cut materials like glass such as drilling, milling, three-dimensional (3D) microstructure fabrication, etc. Besides, very few studies have been delineated regarding the simultaneous multi-response performance analysis of ECDM concerning MRR, HAZ, HT, ROC, and CE for silica material. This is the motivation for the present investigations to optimize the above responses simultaneously during micro-drilling operation on silica material.

2 ECDM Working Operation

A typical ECDM process consists of an electrolytic cell in which the tool electrode, auxiliary electrode, and work material are dipped together in an aqueous solution of an alkaline electrolyte like NaOH or KOH. It is a discharge-based machining process in which the tool electrode is made as a cathode while the auxiliary electrode is made as the anode. Both the electrodes are kept at a separation distance (IEG) of few centimetres as shown in Fig. 1. A constant gap (machining gap) is sustained across the tool electrode and work material for enabling the electrolyte flow underneath the tool electrode. Electrolyte serves two crucial purposes (i) flushing of debris and (ii) ignition of electrochemical reactions. Electrochemical reactions start taking place once the potential difference in a continuous form or pulsed form is applied across both electrodes. As soon the potential difference is applied, the

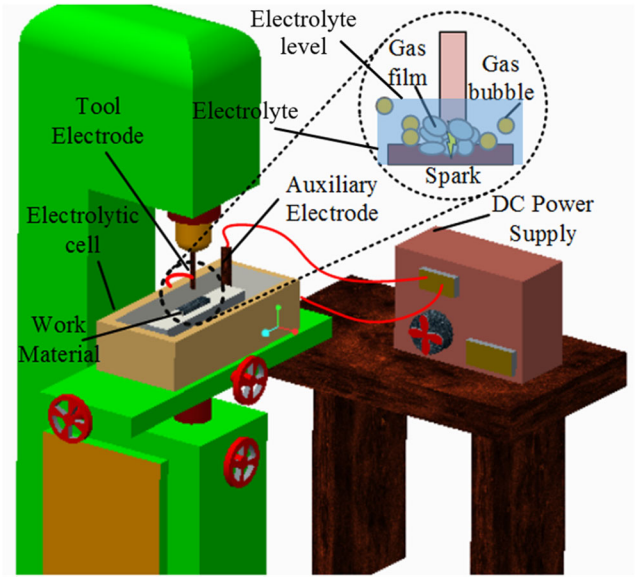

Fig. 1 Schematic diagram of the ECDM working operation

occurrence of the electrolysis process takes place inside the electrolyte. It prompts the evolution of tiny hydrogen bubbles at the cathode-electrolyte interface and tiny oxygen bubbles at the anode electrode respectively. Generally, electrolysis takes place at a lower voltage (typically 20-30 V). The electrochemical reactions at cathode and anode are given below in Eqs. 1 and 2, respectively.

$$2H_2O + 2e^- \rightarrow 2(OH)^- + H_2 \text{ (At cathode)} \quad (1)$$

$$4(OH)^- \rightarrow 2H_2O + O_2 + 4e^- \text{ (At anode)} \quad (2)$$

The rate of evolution of tiny bubbles and their mean radius escalates with the increase in voltage. Subsequently, an isolating gas film is developed at the tool vicinity which acts as a dielectric medium and constricts electrons flow within the circuit. The gas film formation is the result of the amalgamation process of tiny bubbles which touch each other physically. It constrains the current flow and as a result, a spark is generated owing to the electric breakdown of dielectric medium formed in the form of gas film. The gas film quality in terms of its stability and thickness serves a crucial role in determining the dimensional accuracies of machined surface, machining quality, and machining repeatability.

As the applied voltage is increased further, the rate of evolution or formation of tiny bubbles increases further, allowing a gas film to form quickly. Hence, rapid sparks occur with higher intensities at a higher voltage. Spark striking raises the work material's temperature above its melting temperature, which is placed just underneath the tool electrode. Thus, removal of the work material takes place through

melting and vaporization followed by chemical dissolution due to chemical etching. The quality of gas film at the surrounding area of the tool electrode is guided by various controllable parameters such as electrolyte surface tension, electrolyte viscosity, buoyancy force, tool electrode wettability, current densities and thermo-capillary flow due to temperature difference [56].

3 Experimental Design and Machining Setup

The experimental setup for performing experiments is designed, fabricated, and adapted to a vertical milling machine as shown in Fig. 2. The motion of the tool electrode over the work material is consciously controlled through the machine Z-axis having a minimum resolution of 0.05 mm. The electrolytic cell is made up of a non-toxic and non-reactive material that is filled with the required level of alkaline electrolyte to perpetuate an effective machining gap and tool immersion depth. Quartz is chosen as work material for the present study having dimensions 15 × 15 × 1 mm (Key properties are given in Table 1). Quartz work material is fixed on non-reactive fixtures inside the electrolytic cell and gravity assisted tool feed is utilized. A stainless-steel tool electrode with a pointed end having diameter of 0.5 mm is used for drilling micro-holes. NaOH is selected as an electrolyte due to its higher specific conductance. A full-wave and continuous direct current (DC) voltage (0 to 100 V) is used as an energy source and applied across the two electrodes.

3.1 Machining Procedure and Conditions

In the present investigations, the experiments are conducted to identify the optimum combination of parameters for multi-objective responses. The experiments are designed and planned following Taguchi's L9 orthogonal array. Applied voltage (V), electrolyte concentration (wt.%), and IEG (mm) are selected as process parameters at three levels. MRR, HAZ, HT, ROC, and CE are selected as response parameters for analyzing the machining performance. The computed response parameters are analyzed using S/N ratio ("higher the better" for MRR and "smaller the better" for HAZ, HT, ROC, and CE) to establish a combination of optimum parameter levels for individual responses during the machining of quartz work material. Moreover, GRA is used for obtaining multi-response parametric optimization. The contribution of the input process parameters to the desired response parameters is calculated through analysis of variance (ANOVA).

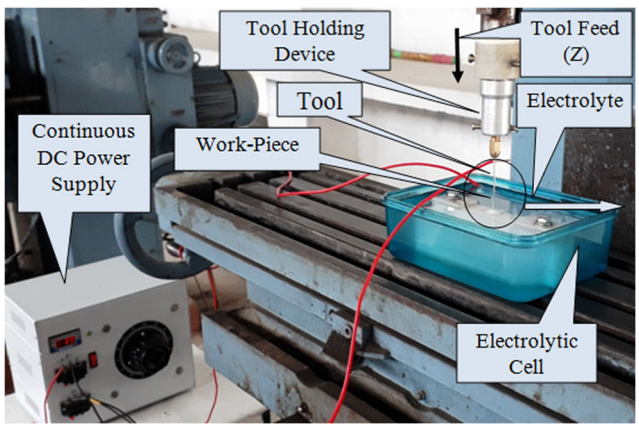

Fig. 2 Developed ECDM set up [57]

Table 1 Crucial Properties of Quartz (SiO_2) [54]

Properties	Value
Chemical Composition	$SiO_2 \geq 99.99$
Thermal Conductivity (at 20 °C)	1.4 (W/m°C)
Density	2.2 X 10^3 kg/m^3
Young's Modulus	7.2×10^{10} Pa
Poisson Ratio's	0.17

The machining conditions used for the present experimental investigation are given in Table 2. The selection of input parameters and their levels for investigation are based on literature domain data, pilot experiments, and experimental set-up capabilities. Initial input parameters for studying the response parameters are randomly selected [58, 59]. They are taken as the applied voltage (35 V), electrolyte concentration (20 wt.%), and IEG (45 mm).

3.2 Measurement of Response Parameters

3.2.1 MRR

MRR is computed by measuring the difference between the weight of Quartz work material before and after machining as given in Eq. 3.

$$\text{MRR} = ((wt_1 - wt_2)/t) \quad (3)$$

where, wt_1 = Quartz work material weight before micro-drilling (g), wt_2 = Quartz work material weight after micro-drilling (g) and t = time in minutes. A weighing machine (Model: CAY220, make: CAS corporation) having a resolution of 0.0001 g is used for measurement. Finally, the volume of material removal is calculated by dividing the MRR with density (g/mm^3) of quartz work material.

$$\text{Volume of material removal} = MRR/density\ (\rho) \quad (4)$$

Table 2 Machining Conditions and levels of input process parameters

Constant Parameters		Variable Parameters				
		Levels		I	II	III
Cathode and Anode Material	Stainless steel	Applied Voltage (V)	A	35	45	55
Tool electrode diameter	500 μm	Electrolyte Concentration (wt./v %)	B	15	20	25
Electrolyte	NaOH	IEG (mm)	C	25	35	45
Electrolyte Level (Approx.)	1 mm above the work material	Machining time (Min)		2		

3.2.2 HAZ

HAZ occurs due to the conduction of the heat on the quartz surface and is computed as the difference across the area (A1) and area of a micro-hole entrance (A2) as shown in Fig. 3a.

$$\mathrm{HAZ} = A1 - A2 \tag{5}$$

3.2.3 HT

In this present investigation, HT is measured as elaborated in Eq. 6 using hole entrance diameter (D_{ent}), hole exit diameter (D_{ext}), and hole depth (h) as shown in Fig. 3c.

$$\mathrm{HT} = \left[\tan^{-1}\left(\frac{D_{ent} - D_{ext}}{2*h}\right)\right] * \pi/180 \tag{6}$$

3.2.4 Roc

ROC is defined as the difference across the measured diameter of the hole entrance (D_{ent}) and the tool electrode diameter (d). An illustration of ROC during the micro-hole drilling process is shown in Fig. 3b.

$$\mathrm{ROC} = D_{ent} - d \tag{7}$$

3.2.5 CE

CE is defined as the 'out of roundness' error. It is used to determine the geometrical accuracy of the hole i.e. circularity and is computed as the difference between the maximum and minimum radius of the hole as shown in Fig. 4 [60, 61].

$$\mathrm{CE} = R_{max} - R_{min} \tag{8}$$

4 Results and Analysis

4.1 S/N Ratio Analysis

S/N ratio is applied to measure the robustness and performance of the process. It analyzes the deviation of the response values from the desired values. The S/N ratio which is a logarithm function is calculated by determining the proportion of the signal to noise. A high S/N ratio indicates the quality of the product which is preferred for decreasing the effects of noise.

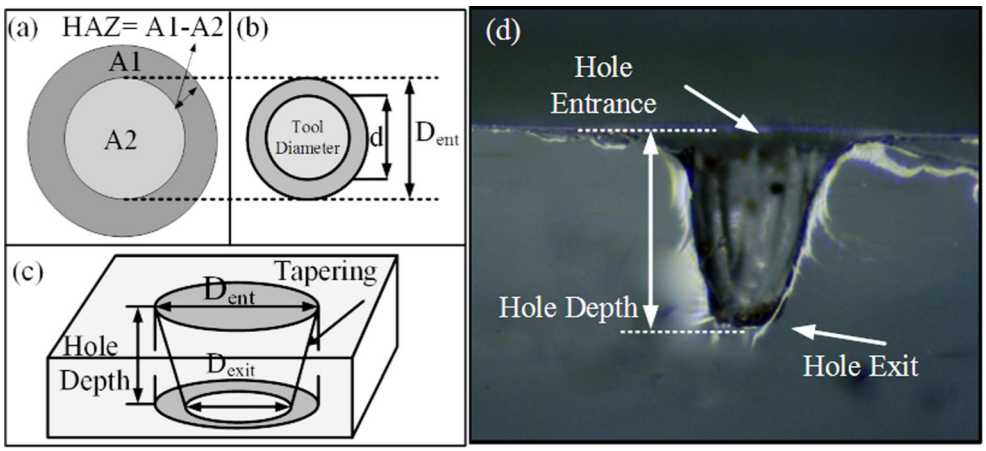

Fig. 3 Schematic diagrams for assessing **a** HAZ **b** ROC **c** HT **d** HT at 35 V, 25 wt.%, 45 mm (*Microscopic Sectional view*)

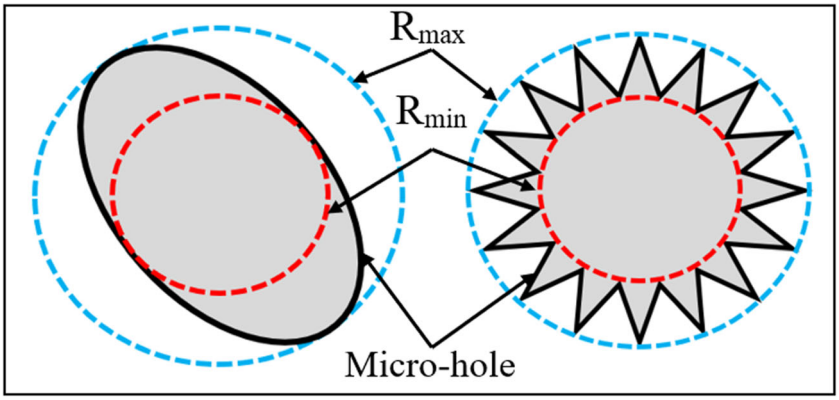

Fig. 4 Schematic diagram for assessing CE [60, 61]

In the present investigation, the "higher-the-better" and "smaller-the-better" approach is utilized for analyzing and optimizing the single response characteristics. The S/N ratios for MRR are computed based on "higher-the-better" as given in Eq. 9.

$$S/N = -10\log_{10}\left[\frac{1}{n}\sum_{i=1}^{n}\left(\frac{1}{MRR_i}\right)^2\right] \quad (9)$$

While the S/N ratios for HAZ, HT, ROC, and CE are computed based on "smaller the better" as given in Eq. 10.

$$S/N = -10\log_{10}\left[\frac{1}{n}\sum_{i=1}^{n}\left((HAZ\ or\ HT\ or\ ROC\ or\ CE)_i\right)^2\right] \quad (10)$$

where i is the current response value and n is the number of response measurements.

The measured response parameters and their computed S/N ratios are given in Table 3. Generally, higher magnitudes of the S/N ratio for a certain combination of process parameters are taken as dominant parameters affecting the response measurements. In this investigation, the delta value is utilized to determine the parameters optimum combination which is seen as the difference of highest and lowest mean S/N ratio. The delta values for three levels of process parameters are shown in Table 4.

4.1.1 Influence of Input Parameters on MRR

Figure 5a shows the graph plot of the mean S/N ratio for MRR. Figure 6a-c illustrates the surface plots of MRR versus applied voltage, electrolyte concentration, and IEG while Fig. 6d shows the trend of MRR variation with respect to input process parameters corresponding to experiment numbers 1–9.

It is observed that the MRR increases with the increase in applied voltage (Figs. 5a, 6a and b) and electrolyte concentration (Figs. 5a, 6a and c). Any increase in applied voltage results in magnifying the density of gas bubbles that enhances the spark intensity over the work material. As a result, more material removal occurs due to high thermal energy input. For the same level of electrolyte concentration at 15 wt.%, the MRR increases from 0.5291mm^3/min to 1.1365 mm^3/min with the increase in voltage from 35 V to 55 V (Fig. 6a and d, experiment numbers 1, 4 & 7).

An increase in electrolyte concentration enhances the hydroxide ions (OH) which increases its electrical conductivity.

Table 3 Experimental design and Response measurements with S/N ratios

Exp	(V)	(wt. /v. %)	IEG (mm)	MRR (mm^3/min)	S/N Ratio MRR (dB)	HAZ (mm^2)	S/N Ratio HAZ (dB)	HT (radian)	S/N Ratio HT (dB)	ROC (mm)	S/N Ratio ROC (dB)	CE (mm)	S/N Ratio ROC (dB)
1	35	15	25	0.5291	−5.5292	0.2064	13.7058	0.1761	15.0848	0.0063	44.0132	0.0967	20.2915
2	35	20	35	0.5614	−5.0146	0.3861	8.266	0.1696	15.4115	0.0375	28.5194	0.1369	17.2719
3	35	25	45	0.6254	−4.0768	0.6002	4.4341	0.1938	14.2529	0.0498	26.0554	0.1224	18.2444
4	45	15	35	0.6046	−4.3706	0.4990	6.038	0.1706	15.3604	0.0282	30.995	0.1276	17.8830
5	45	20	45	0.8706	−1.2036	0.5783	4.7598	0.2156	13.327	0.0702	23.0733	0.1302	17.7078
6	45	25	25	1.0989	0.8192	0.5456	5.2625	0.2199	13.1555	0.0819	21.7343	0.1662	15.5874
7	55	15	45	1.1365	1.1114	0.4317	7.2964	0.1817	14.8129	0.0629	24.027	0.1059	19.5021
8	55	20	25	1.1495	1.2102	0.4160	7.6181	0.2291	12.7995	0.1394	17.1147	0.1144	18.8315
9	55	25	35	1.1044	0.8625	0.5873	4.6228	0.2686	11.4179	0.1273	17.9034	0.1597	15.9339

Table 4 Mean S/N ratio and computed delta values for MMR, HAZ, HT, ROC, and CE

	MRR mean S/N Ratio			HAZ mean S/N Ratio		
Level	Applied Voltage (A)	Electrolyte Concentration (B)	IEG (C)	Applied Voltage (A)	Electrolyte Concentration (B)	IEG (C)
1	−4.8735	−2.9295	**−1.1666**	**8.802**	**9.013**	**8.862**
2	−1.585	−1.6693	−2.8409	5.352	6.880	6.309
3	**1.0614**	**−0.7984**	−1.3897	6.512	4.773	5.496
Delta	5.94	2.14	1.68	3.45	4.24	3.37
Rank	**1**	**2**	**3**	**2**	**1**	**3**
	HT mean S/N Ratio			**ROC mean S/N Ratio**		
Level	Applied Voltage (A)	Electrolyte Concentration (B)	IEG (C)	Applied Voltage (A)	Electrolyte Concentration (B)	IEG (C)
1	**14.92**	**15.09**	13.68	**32.86**	**33.01**	**27.62**
2	13.95	13.85	14.06	25.27	22.9	25.81
3	13.01	12.94	**14.13**	19.68	21.9	24.39
Delta	1.91	2.14	0.45	13.18	11.11	3.24
Rank	**2**	**1**	**3**	**1**	**2**	**3**

CE mean S/N Ratio

Level	Applied Voltage (A)	Electrolyte Concentration (B)	IEG (C)
1	**18.60**	**19.23**	18.24
2	17.06	17.94	17.03
3	18.09	16.59	**18.48**
Delta	1.54	2.64	1.46
Rank	**2**	**1**	**3**

It prompts an increase in current density and rate of formation of bubbles that further enhances the formation rate of gas film. As a result, high frequencies of sparks occur and, in this way, increases the MRR. For the same level of applied voltage at 45 V, the MRR increases from 0.6046 mm^3/min to 1.0989 mm^3/min with the increase in electrolyte concentration from 15 wt.% to 25 wt.% (Fig. 6a and d, experiment numbers 4, 5 & 6). Lastly, the IEG enables the electric current flow within the circuit. Any increase in the IEG causes the decrease of electric current flow due to an increased resistance across the path. Therefore, MRR reduces with an increase in IEG [13].

But, it is observed that MRR decreases with the increases in IEG from 25 mm to 35 mm while it increases with the further increase in IEG from 35 mm to 45 mm (Figs. 5a, 6b and d at 45 V). It is because applied voltage and electrolyte concentration has more effect on the MRR when compared to IEG. Sarkar et al. [13] mentioned that influential parameter dominates over another less influential parameter in determining the responses at different machining level. In this case, MRR increases from 0.6046 mm^3/min to 0.8706 mm^3/min with the increase in IEG from 35 mm to 45 mm due to the increase in electrolyte concentration from 15 wt.% to 20 wt.% at a higher voltage level of 45 V (Figs. 5a, 6c and d, experiment numbers 4 & 5, Table 3).

Figure 6d shows that maximum MRR (1.1495 mm^3/min) is obtained at experiment number 8 (55 V, 20 wt.%, 25 mm) while minimum MRR (0.5291mm^3/min) is obtained at experiment number 1 (35 V, 15 wt.%, 25 mm). This increase is observed due to an increase in applied voltage and electrolyte concentration. The corresponding microscopic images of micro-holes machined on quartz work material at experiment number 1 and 8 are shown in Fig. 7. It is seen that hole entrance radius increases at experiment number 8 (339.317 μm) when compared to the hole entrance radius at experiment number 1 (206.283 μm) which indicates that high material removal occurs. Outer circle (OC) radius and inner circle (IC) radius are used to compute HAZ, ROC, and HT (Fig. 3). IC radius is used for calculating hole entrance diameter (D_{ent}).

4.1.2 Individual Response Optimization for MRR

From the delta values given in Table 4, it has been observed that MRR is influenced by applied voltage (Rank 1, highest: 5.94), followed by electrolyte concentration (Rank 2, 2.14) and then an IEG (Rank 3, lowest: 1.68). For maximizing the MRR, the combination of optimum process parameters come out to be A3B3C1 i.e. (55 V, 25%, 25 mm) (Fig. 5a). Higher values of applied voltage and electrolyte concentration bring about the increased densities of hydrogen gas bubbles which

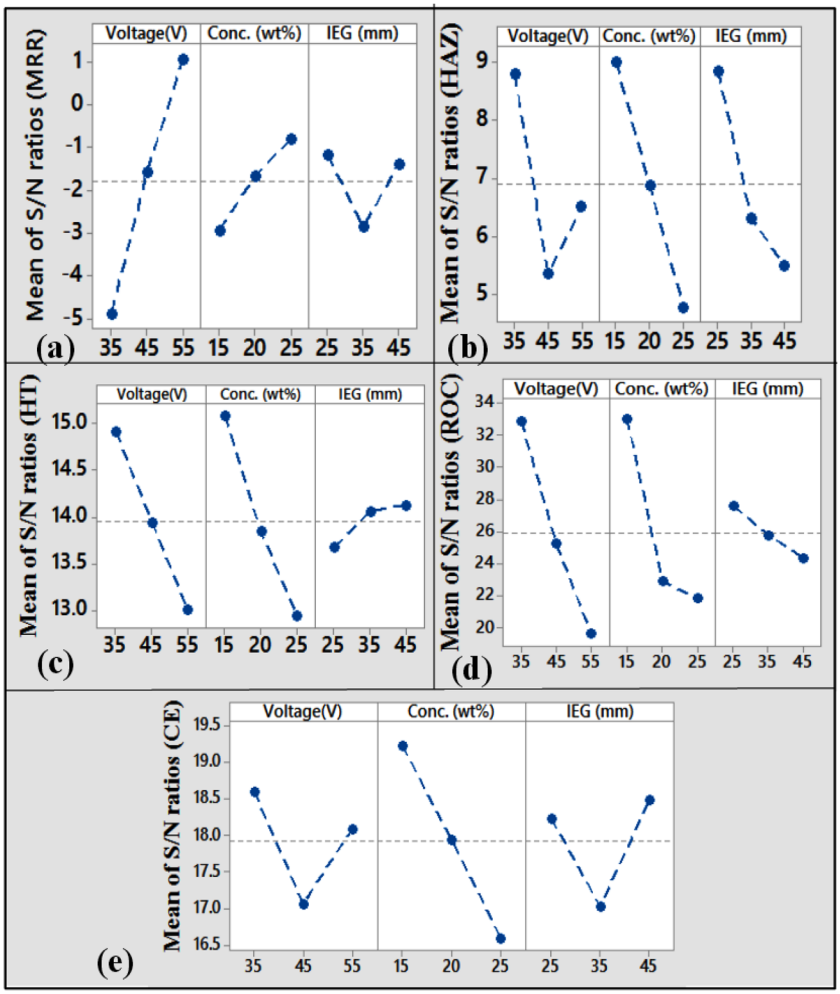

Fig. 5 Plot of mean S/N ratio for response parameters **a** MRR, **b** HAZ, **c** HT, **d** ROC, **e** CE

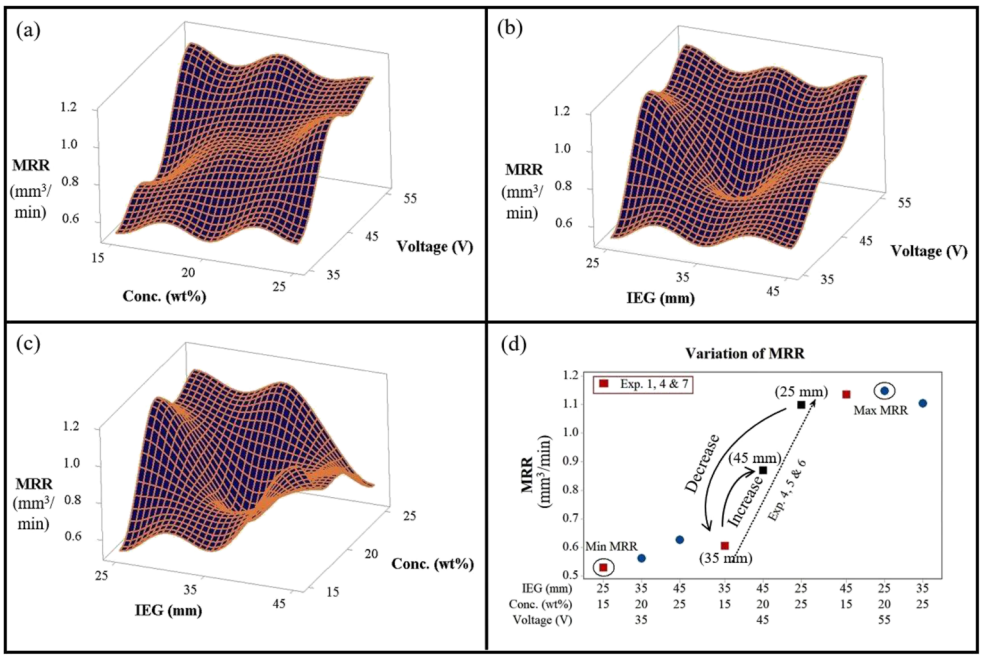

Fig. 6 **a**-**c** MRR surface plots **d** Variation of MRR with respect to input process parameters

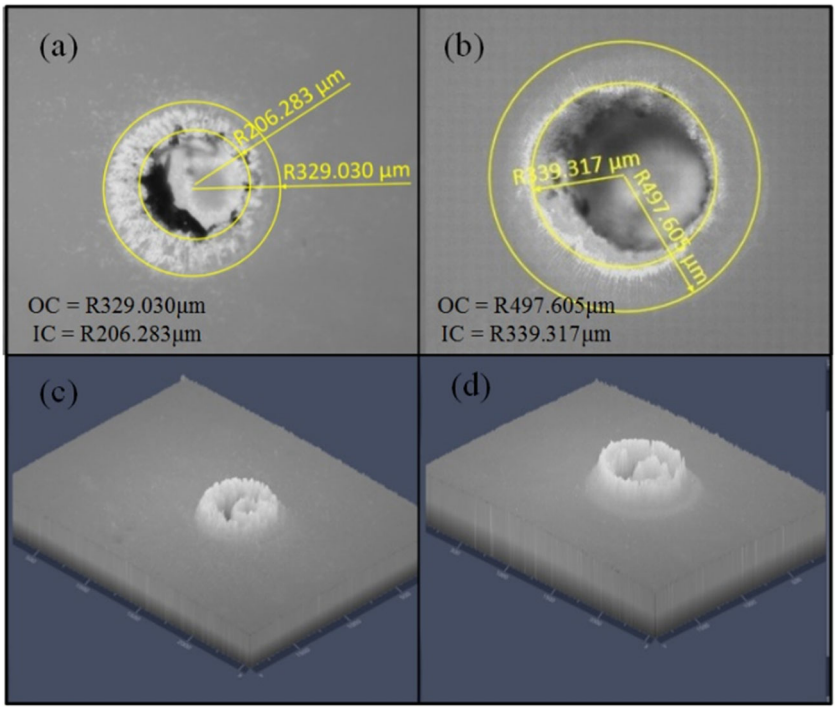

Fig. 7 Microscopic images of machined quartz work material at 35 V, 15 wt%, 25 mm (**a**) in 2D, (**c**) in 3D and at 55 V, 20 wt%, 25 mm (**b**) in 2D, (**d**) in 3D; OC is outer circle radius, IC is inner circle radius

empower the quick gas film formation around the tool surrounding area. Lower IEG values provide higher current intensities across the circuit with less resistance. Subsequently, this combination upgrades the frequency of sparks over the work material surface. Hence, high MRR was acquired.

Thereafter, ANOVA is performed to identify the percentage contribution of each input parameter to the MRR response as given in Table 5. It is observed that applied voltage has the highest contribution to the MRR with a 78.46% percentage followed by electrolyte concentration, with 8.77% and then IEG with 7.63%.

4.1.3 Influence of Input Parameters on HAZ

Figure 5b shows the graph plot of the mean S/N ratio for HAZ. Figure 8a-c illustrates the surface plot of HAZ versus applied voltage, electrolyte concentration, and IEG while Fig. 8d shows the trend of HAZ variation with respect to input process parameters corresponding to experiment numbers 1–9. It has been observed that HAZ is the result of thermal heat conducted to the quartz work material at the surrounding area of the micro-holes. Figures 5b, 8a and b) depicted that HAZ increases with the increase in applied voltage from 35 V to 45 V but decreases with the further increase in voltage from 45 V to 55 V. Increase in voltage results into the increase in thermal energy per spark (as discussed in section 4.1.1). This enhances the heat energy input to the work material and as a result, high HAZ is acquired. A further decrease in HAZ with the increase in HAZ from 45 V to 55 V is accounted for the fact that electrolyte concentration dominates the HAZ (Rank 1, Table 4) over applied voltage. Figure 8d indicates that for experiment number 3 (35 V, 25 wt.%, 45 mm) and experiment number 7 (55 V, 15 wt.%, 45 mm), there is a decrease in HAZ from 0.6002 mm^2 to 0.4317 mm^2 due to a decrease in electrolyte concentration from 25 wt.% to 15 wt.%.

It is observed that HAZ increases with the increase in electrolyte concentration (Fig. 8a, c and d) owing to the increase in electrical conductivity which raises the spark intensity over

Table 5 ANOVA results for MRR

Parameters	DOF	Sum of Squares	Variance	F-Value	Percentage Contribution (%)
Applied Voltage	2	0.46742	0.23371	15.28	**78.46**
Electrolyte Concentration	2	0.05222	0.02611	1.71	8.77
IEG	2	0.04548	0.02274	1.49	7.63
Error	2	0.03059	0.01530		5.14
Total	8	0.59571			

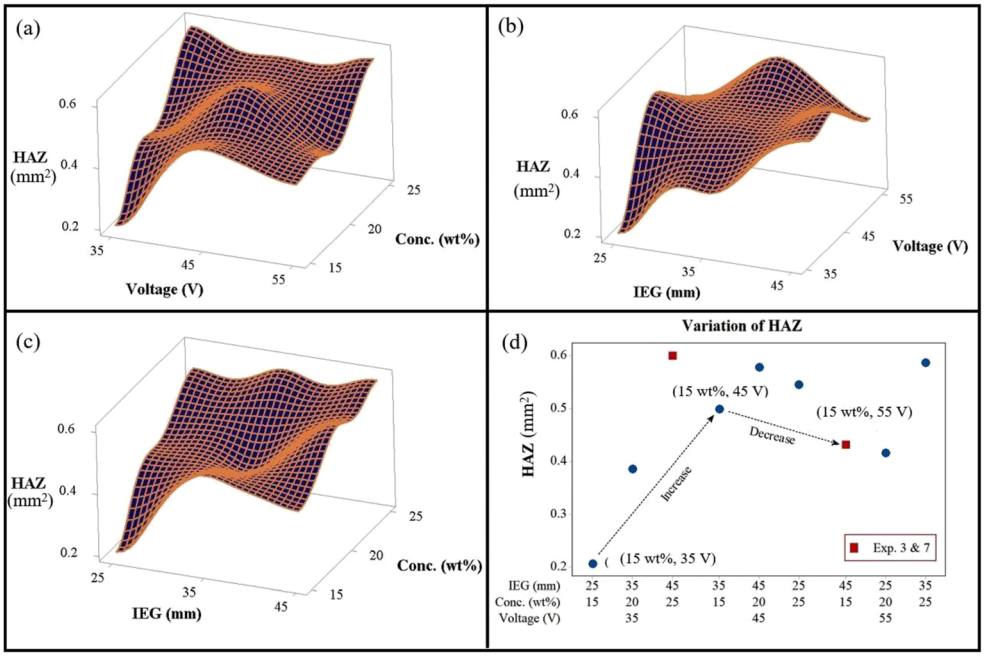

Fig. 8 **a-c** HAZ surface plots **d** Variation of HAZ with respect to input process parameters

the work material. Subsequently, more thermal energy is obtained in the machining zone and hence high HAZ. Figure 9 shows the microscopic images of machined micro-holes on work material at 35 V which illustrates an increase in HAZ with the increase in electrolyte concentration at three different levels i.e., 15 wt.% (Fig. 9a), 20 wt.% (Fig.9b), 25 wt.% (Fig.9c).

HAZ is least affected by the IEG (Rank 3). Figure8b-c shows that HAZ increases with the increase in an IEG despite an increase in path resistance. It is explained by the fact that electrolyte concentration dominates over IEG during the machining process which produces high HAZ at higher IEG level (Table 3). Figure 8d shows that for experiment number 4 (45 V, 15wt.%, 35 mm) & 5 (45 V, 25wtz.%, 45 mm), HAZ increases from 0.4990mm^2 to 0.5783 mm^2 with the increase in IEG from 35 mm to 45 mm due to increase in electrolyte concentration from 15 wt.% to 20 wt.%. A similar trend is observed for experiment numbers 1, 2 & 3.

4.1.4 Individual Response Optimization for HAZ

The combination of optimum process parameters for minimum HAZ comes out to be A1B1C1 i.e. (35 V, 15%, 25 mm) as given in Table 4 and graphical plot of a mean of S/N ratio (Fig. 5b). Further, delta values reveal that HAZ is strongly influenced by electrolyte concentration (Rank 1,

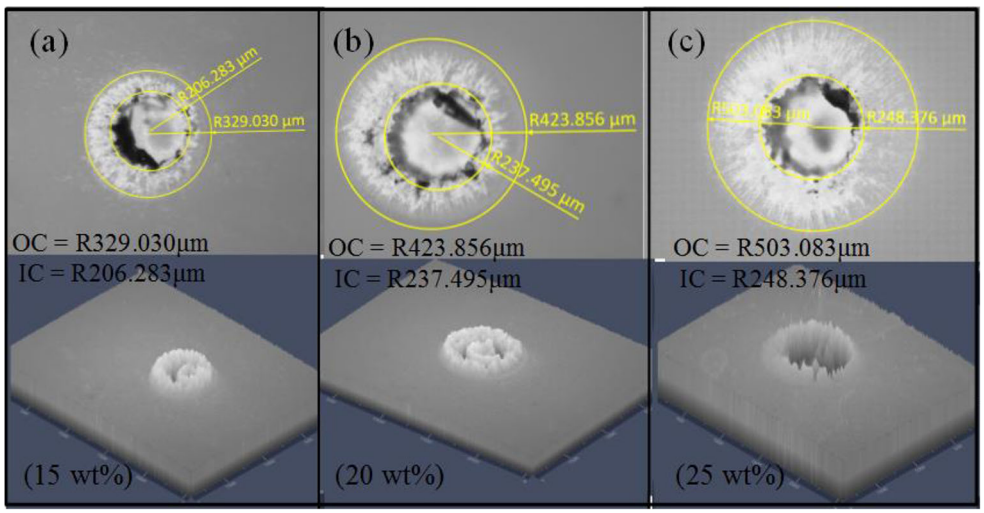

Fig. 9 Microscopic images of increasing HAZ at different electrolyte concentration **a** 2D, 15 wt% **b** 2D, 20 wt.% **c** 2D, 25 wt.% **d** 3D, 15 wt% **e** 3D, 20 wt.% **f** 3D, 25 wt.%; OC is outer circle radius, IC is inner circle radius

Table 6 ANOVA results for HAZ

Parameters	DOF	Sum of Squares	Variance	F-Value	Percentage Contribution (%)
Applied Voltage	2	0.031010	0.015505	6.40	23.88
Electrolyte Concentration	2	0.059868	0.029934	12.35	**46.11**
IEG	2	0.034132	0.017066	7.04	26.28
Error	2	0.004847	0.002424		3.73
Total	8	0.129856			

highest: 4.24) followed by applied voltage (Rank 2, 3.45) and then an IEG (Rank 3, lowest: 3.37). This combination can be explicated on an account that at lower electrolyte concentration and applied voltage, the frequency of the sparks is reduced. Thus, energy transference to the work material is less at lower levels of electrolyte concentration and applied voltage which further reduces HAZ. Lastly, HAZ is determined to be least affected by the IEG and observed minimum at its lowest level. The presence of the debris may increase the inter-electrode resistance in the flow path which produces less HAZ at a low level of IEG.

ANOVA results (Table 6) reveal that electrolyte concentration has the highest contribution to the HAZ with 46.11% followed by IEG with 26.28% and then applied voltage with 23.88%.

4.1.5 Influence of Input Parameters on HT

Figure 5c shows the graph plot of the mean S/N ratio for HT. Figure 10a illustrates the surface plot of HT versus applied voltage, electrolyte concentration, and IEG while Fig. 10a-d shows the trend of HT variation with respect to input process parameters corresponding to experiment numbers 1–9. HT is measured as the difference between the diameters of hole entrance and hole exit along with the hole depth. A cross-sectional microscopic image of micro-hole demonstrates the HT is shown in Fig. 3d. Figure 10a, b and d shows that HT increases with the increase in applied voltage because more thermal energy is obtained in the machining zone. The increase in HT is perceived due to an increase in the hole entrance diameter. It has been noticed that hole entrance diameter increases more with the increase in an applied voltage due to an increase in the formation rate of gas film. It produces a high frequency of sparks over the work material top surface and leads to more material removal.

Figure 11 illustrates an increase in hole entrance diameter with the increase in applied voltage from 35 V to 55 V during micro-hole machining at 20 wt.% (experiment numbers 2, 5 & 8). Any increase in hole entrance diameter has a great effect on HT when compared to hole

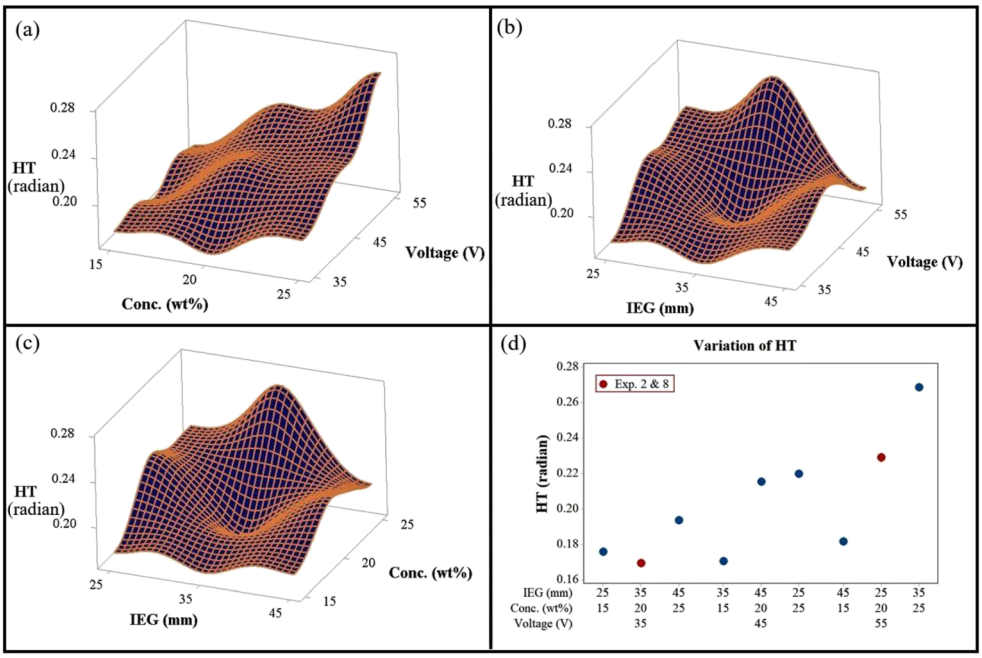

Fig. 10 **a-c** HT surface plots **d** Variation of HT with respect to input process parameters

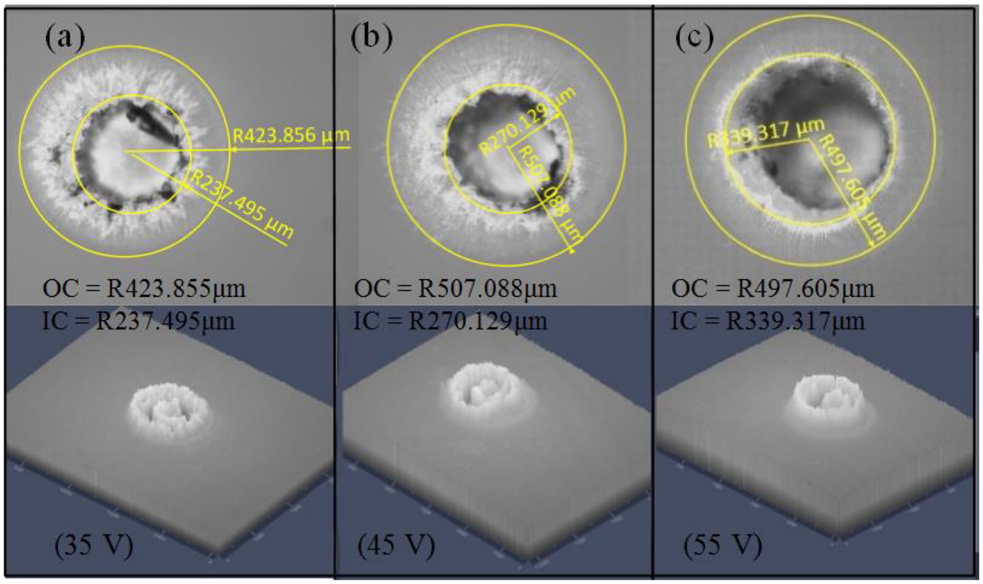

Fig. 11 Microscopic images of increasing hole entrance diameter (D_{ent}) at different applied voltage **a** 2D, 35 V **b** 2D, 45 V **c** 2D, 55 V **d** 3D, 35 V **e** 3D, 45 V **f** 3D, 55 V; OC is outer circle radius, IC is inner circle radius

exit diameter because of the prolonged exposure of the work material top surface to the sparks. As a result, an increase in HT is observed with the increase in applied voltage. For a constant electrolyte concentration of 20 wt.%, HT increases from 0.1696 rad to 0.2291 rad with the increase in applied voltage from 35 V to 55 V (experiment numbers 2 & 8, Fig. 10a and d).

Figure 10a, c and d illustrates that an increase in electrolyte concentration contributes to an increase in HT as, at higher concentration of electrolyte, more electrochemical reactions and sparks occur over the work material's top surface i.e. at hole entrance when compared to hole exit diameter. Chemical etching action also contributes to the removal of the material. More OH ions are available on the work material's top surface

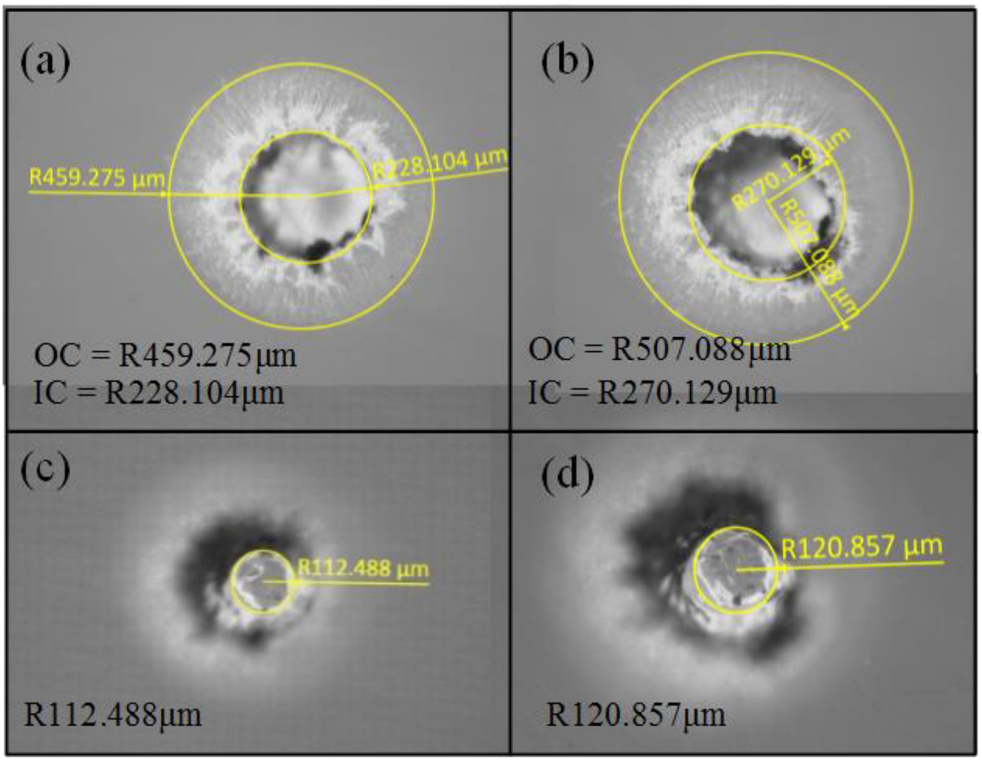

Fig. 12 Comparison of hole entrance and exit diameters at 45 V **a** D_{ent} at 15 wt%, 35 mm **b** D_{ent} at 20 wt%, 45 mm **c** D_{ext} at 15 wt%, 35 mm **d** D_{ext} at 20 wt%,45 mm; OC is outer circle radius, IC is inner circle radius

Table 7 ANOVA results for HT

Parameters	DOF	Sum of Squares	Variance	F-Value	Percentage Contribution (%)
Applied Voltage	2	0.003264	0.001632	2.28	36.86
Electrolyte Concentration	2	0.003965	0.001983	2.77	**44.78**
IEG	2	0.000193	0.000096	0.13	2.18
Error	2	0.001433	0.000717		16.18
Total	8	0.008856			

at higher electrolyte concentration which enhances the etching action.

There is a lack of availability of the electrolyte at the higher depth resulting in lower material removal at hole exit comparative to hole entrance. Figure 12 compares the diameter of hole entrance and hole exit at 15 wt.% and 20 wt.% electrolyte concentration during machining at 45 V (experiment numbers 4 & 5). It indicates that both the diameter increases with the increase in electrolyte concentration but an increase in exit diameters are less when compared to the increase in entrance diameters. Figure 10c shows that HT decreases with the increase in the IEG due to an increase in IEG resistance. It decreases the spark intensities over the work material and removes less material.

4.1.6 Individual Response Optimization for HT

HT is strongly influenced by the electrolyte concentration (Rank 1, Highest: 2.14) followed by applied voltage (Rank 2, 1.91) and then an IEG (Rank 3, Lowest: 0.45). The combination of optimum process parameters for minimum HT comes out to be A1B1C3 i.e. (35 V, 15%, 45 mm) (Fig. 5c). At higher levels of voltage and electrolyte concentration, there is an enlargement in hole entrance diameter which elevates the taper in the micro-hole drilling process. The disparity of OH ions along with the hole depth also results in variable etching action as the tool moves into the work material. Consequently, there is a difference in hole entrance and exit diameter. Hence, lower values of applied voltage and electrolyte concentration lead to reduced HT.

Higher IEG level escalates the inter-electrode resistance that further reduces the electrolyte's conductivity. Subsequently, it removes less material at the hole entrance and reduces HT. ANOVA results (Table 7) reveal that electrolyte concentration has the highest contribution to the HT with 44.78% followed by the applied voltage, with 36.86% and then IEG with 2.18%.

4.1.7 Influence of Input Parameters on ROC

Figure 5d shows the graph plot of the mean S/N ratio for ROC. Figure 13a-c illustrates the surface plot of ROC versus applied voltage, electrolyte concentration, and IEG while Fig. 13d

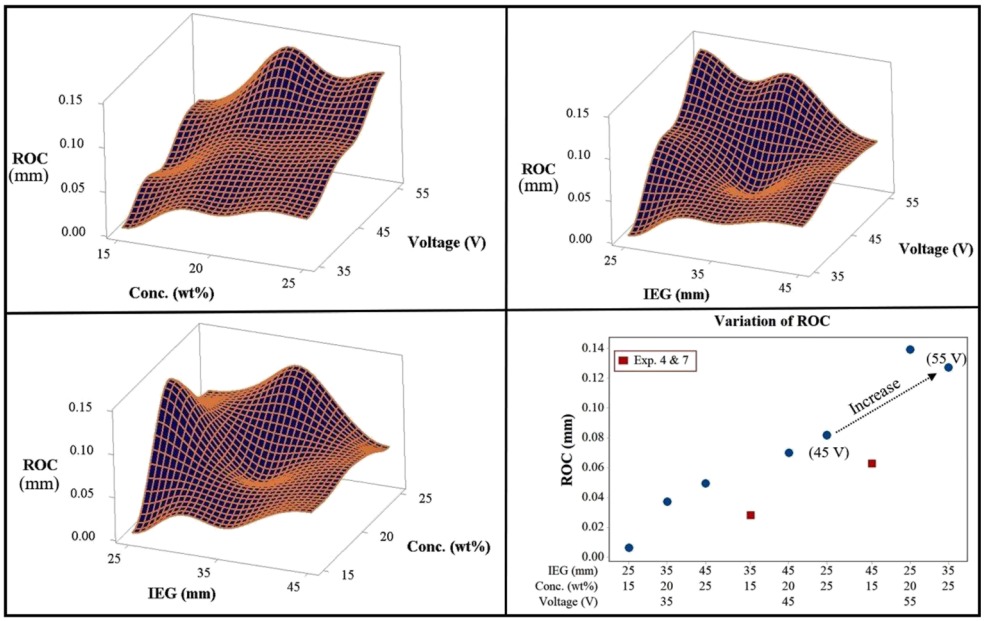

Fig. 13 **a-c** ROC surface plots (**d** Variation of ROC with respect to input process parameters

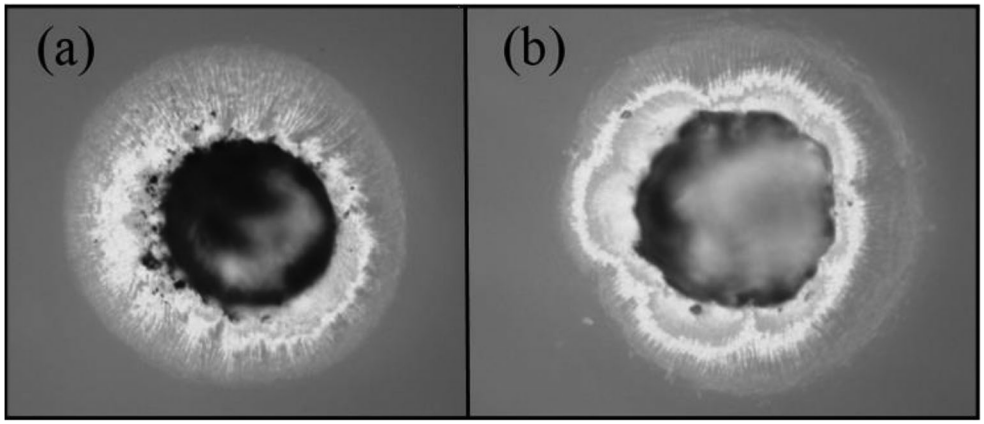

Fig. 14 Hole quality at **a** 45 V **b** 55 V

shows the trend of ROC variation with respect to input process parameters corresponding to experiment numbers 1–9.

It is depicted that ROC increases with the increase in applied voltage (Fig. 13a and b) and electrolyte concentration (Fig. 13c). With the increasing values of applied voltage and electrolyte concentration, the quality of the drilled hole deteriorates, i.e. there is an increase in ROC. Figure 14 shows the quality of micro-hole drilled at two different voltages. ROC increases from 0.0819 mm to 0.1273 mm when the voltage increases from 45 V to 55 V (Figs. 13d and 14, experiment numbers 6 & 9). The reason, thereof, is seen as the high frequency of sparks occur from the sides of the tool electrode at higher levels of applied voltage and electrolyte concentration [31]. Thermal energy given by the sparks in the ECDM process is proportional to the concentration of OH ions, which increases with the increase in electrolyte concentration [13]. Also, more chemical etching action is observed at the hole edges, thereby resulting in increased ROC.

ROC is supposed to decrease with the increase in the IEG due to an increase in inter-electrode resistance. But the opposite trend is observed in the case of the IEG (Fig. 13c) which may be explained by the fact that applied voltage (Rank 1) and electrolyte concentration (Rank 2) dominate over IEG during the machining process which produces high ROC at higher IEG level. ROC increases from 0.0282 mm to 0.0629 mm with the increase in IEG from 35 mm to 45 mm due to the increase in applied voltage from 45 V to 55 V (Fig. 13d, experiment numbers 4 & 7).

4.1.8 Individual Response Optimization for ROC

ROC is strongly influenced by the applied voltage (Rank 1, Highest: 13.18) followed by the electrolyte concentration (Rank 2, 11.11) and then an IEG (Rank 3, Lowest: 3.24). The combination of optimum process parameters for minimum ROC comes out to be A1B1C1 i.e. (35 V, 15%, 25 mm) (Fig. 5d). A lower level of both applied voltage and electrolyte concentration mitigates the spark intensity from the sides of the tool. As a result, heat energy per unit spark also reduces. The effect of a lower level of the IEG has been discussed earlier (Section 4.1.4), the presence of debris increases the resistance across the electrodes and minimize the removal rate at the hole edges. ANOVA results (Table 8) reveal that applied voltage has the highest contribution to the ROC with 61.36% followed by electrolyte concentration, with 34.92% and then IEG with 2.37%.

4.1.9 Influence of Input Parameters on CE

Figure 5(e) shows the graph plot of the mean S/N ratio for CE. Figure 15a-c illustrates the surface plots of CE versus applied voltage, electrolyte concentration, and IEG while Fig. 15d

Table 8 ANOVA results for ROC

Parameters	DOF	Sum of Squares	Variance	F-Value	Percentage Contribution (%)
Applied Voltage	2	0.009500	0.004750	45.5	**61.36**
Electrolyte Concentration	2	0.005407	0.002704	25.9	34.92
IEG	2	0.000366	0.000183	1.75	2.37
Error	2	0.000209	0.000104		1.35
Total	8	0.015483			

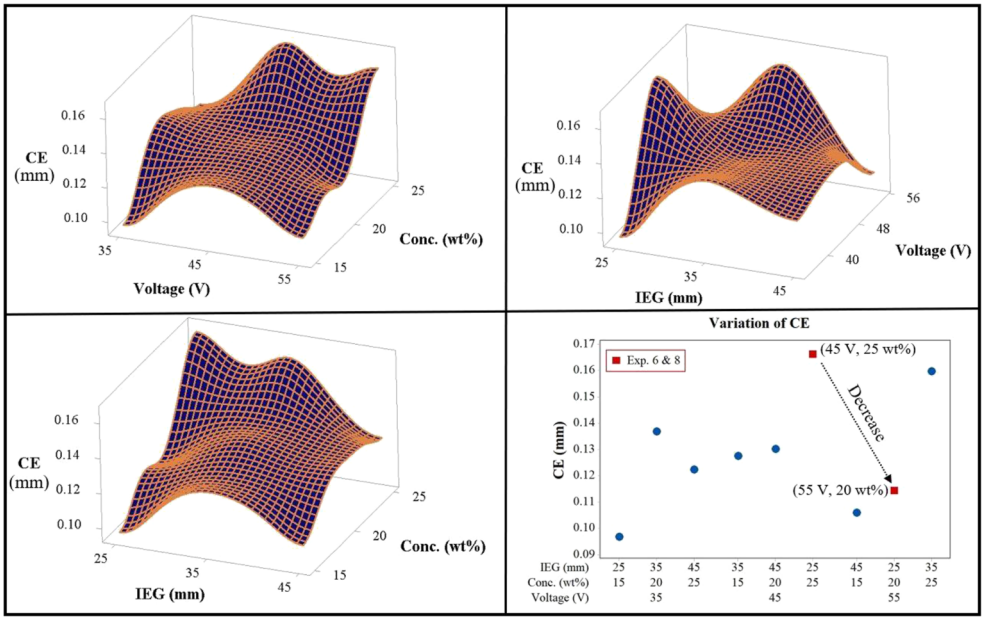

Fig. 15 **a-c** CE surface plots **d** Variation of CE with respect to input process parameters

shows the trend of CE variation with respect to input process parameters corresponding to experiment numbers 1–9. It has been observed that CE increases with the increase in applied voltage (Figs. 5e, 15a and b) due to the improved thermal energy strength over the work material that leads to an increase in CE. However, Figs. 5e and 15a shows that CE increases from 35 V to 45 V and then decreases with a further increase in voltage from 45 V to 55 V. It may be seen due to the dominance of electrolyte concentration over voltage. CE decreases from 0.1662 mm to 0.1144 mm with the decrease in electrolyte concentration from 25 wt.% to 20 wt.% despite an increase in voltage from 45 V to 55 V (Fig. 15a and d, experiment no 6 & 8). Electrolyte concentration is the most influential parameter for controlling CE (Rank 1).

CE increases with an increase in electrolyte concentration (Fig. 15a and c). The more bubble densities are observed in the machining zone with the increase in concentration since the conductivity of electrolyte increases. Consequently, rapid gas film formation and more sparking take place. CE increases with the increase in IEG from 25 mm to 35 mm and then decreases with the further increase in IEG from 35 mm to 45 mm (Figs. 5e and 15b). Electrolyte concentration dominates over the IEG to control the CE. Figure 15c and d shows an increase in CE from 0.0967 mm to 0.1369 with the increase in IEG from 25 mm to 35 mm due to the increase in electrolyte concentration from 15 wt.% to 20 wt.% at 35 V (experiment numbers 1 & 2).

It is stated that a constant force is acting between the tool and work material due to their physical contact in the gravity feed tool system. This may result in the deflection or bending of the tool electrode because the tool size is thin [1]. The reason for CE is mainly accounted for the fact of tool deflection. Subsequently, more sharp edges occur at the micro-hole geometry due to the tool side wall's contact with the work material.

4.1.10 Individual Response Optimization for CE

CE is strongly influenced by the electrolyte concentration (Rank 1, Highest: 2.64) followed by the applied voltage (Rank 2, 1.54) and then an IEG (Rank 3, Lowest: 1.46). The best optimum combination of process parameters for minimum CE comes out to be A1B1C3 i.e. (35 V, 15%, 45 mm) (Fig. 5e). At lower levels of applied voltage and electrolyte

Table 9 ANOVA results for CE

Parameters	DOF	Sum of Squares	Variance	F-Value	Percentage Contribution (%)
Applied Voltage	2	0.000793	0.000396	2.39	18.76
Electrolyte Concentration	2	0.002338	0.001169	7.05	**55.32**
IEG	2	0.000763	0.000382	2.30	18.05
Error	2	0.000332	0.000166		7.87
Total	8	0.004226			

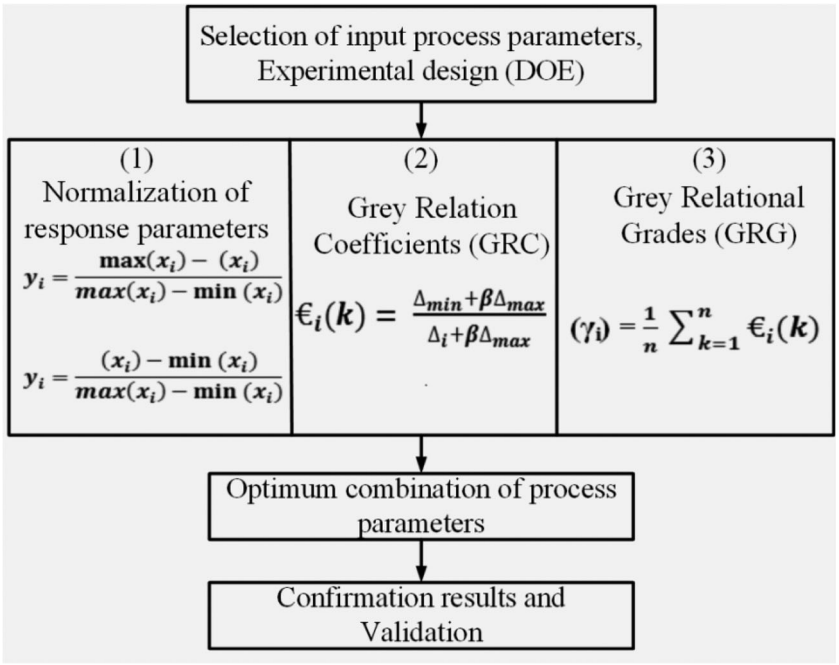

Fig. 16 Steps in GRA

concentration, there is a decrease in the frequencies of the sparks. The higher IEG increases the inter-electrode resistance and hinders the flow of current. This combination reduces the thermal energy transference to the work material and produces low CE.

ANOVA results (Table 9) reveal that electrolyte concentration has the highest contribution to CE with 55.32% followed by the applied voltage, with 18.76% and then IEG with 18.05%.

5 Multi-Response Optimization

It is seen that all the response parameters i.e., MRR, HAZ, HT, ROC, and CE get affected by any change in the input process parameters. S/N ratio results reveal that the maximum MRR is obtained at higher levels of applied voltage, electrolyte concentration, and lower level of IEG i.e., A3B3C1 (Fig. 5, Table 4). While for HAZ, HT, ROC, and CE, the optimum values of process parameters come out be A1B1C1, A1B1C3, A1B1C1, and A1B1C3 respectively (Corresponding delta values and ranking are given in Table 4). Based on ranks, electrolyte concentration is found to be the most influential parameter for HT, HAZ, and CE while applied voltage is found to be most influential for MRR and ROC. Thus, it is very strenuous to analyze which optimum parameter's combinations are to be selected together for multi-objective optimization of response parameters. So, to overcome this problem, a multi-objective optimization technique known as GRA is utilized to identify the combination of the optimum parameters.

Table 10 Normalized values, GRCs, and GRGs for Response parameters

Exp.	Normalized value					GRC					GRG	
	MRR	HAZ	HT	ROC	CE	MRR	HAZ	HT	ROC	CE	Value	Order
1	0.0000	1.0000	0.9343	1.0000	1.0000	0.3333	1.0000	0.8839	1.0000	1.0000	0.8434	1
2	0.0521	0.5437	1.0000	0.7656	0.4216	0.3453	0.5228	1.0000	0.6808	0.4636	0.6025	4
3	0.1552	0.0000	0.7556	0.6732	0.6302	0.3718	0.3333	0.6716	0.6047	0.5749	0.5113	6
4	0.1217	0.2570	0.9899	0.8355	0.5554	0.3628	0.4022	0.9802	0.7524	0.5293	0.6054	3
5	0.5505	0.0556	0.5354	0.5199	0.5180	0.5266	0.3462	0.5183	0.5102	0.5092	0.4821	8
6	0.9184	0.1386	0.4919	0.4320	0.0000	0.8598	0.3673	0.4960	0.4682	0.3333	0.5049	7
7	0.9790	0.4279	0.8778	0.5748	0.8676	0.9598	0.4664	0.8036	0.5404	0.7907	0.7122	2
8	1.0000	0.4678	0.3990	0.0000	0.7453	1.0000	0.4844	0.4541	0.3333	0.6625	0.5869	5
9	0.9273	0.0328	0.0000	0.0909	0.0935	0.8731	0.3408	0.3333	0.3548	0.3555	0.4515	9

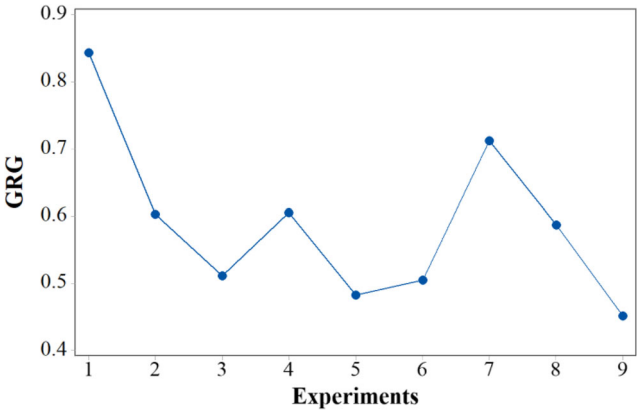

Fig. 17 GRGs at different experiments

5.1 GRA

In GRA, the optimization of multi-objective response parameters is obtained by changing it into a single-objective optimization problem. The step by step procedure for performing the GRA during multi-response optimization is highlighted in Fig. 16. The GRA process includes three phases: (i) Grey Relational Generation (ii) Grey Relational Coefficients (GRC), and (iii) Grey Relational Grades (GRDs). In a grey relational generation, the experimental results of all the response parameters are first normalized using Eqs.11 and 12 respectively. It is performed to get the comparable sequence in the range of 0–1 [62–64]. The measured responses are grouped into two characteristics, namely, "Higher-the-better" and "Smaller-the-better". For normalizing the responses with the "Higher-the-better" approach like MRR, Eq. 11 is used while for normalizing the responses with a "Smaller-the-better" approach like HAZ, HT, ROC, and CE, Eq.12 is used.

$$y_i = \frac{\max(x_i) - (x_i)}{max(x_i) - \min(x_i)} \tag{11}$$

$$y_i = \frac{(x_i) - \min(x_i)}{max(x_i) - \min(x_i)} \tag{12}$$

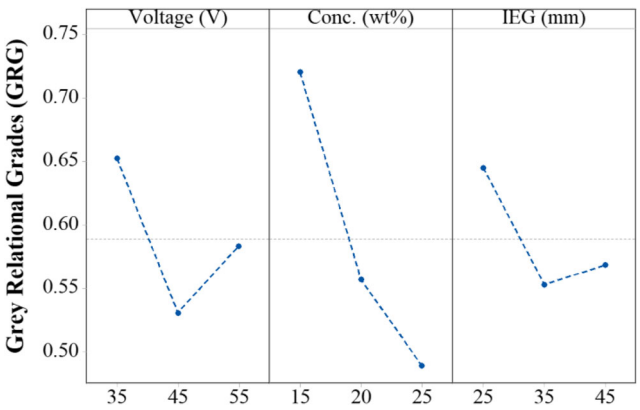

Fig. 18 A plot of mean GRG

Table 11 Mean of GRG and substantial rank

Mean GRG			
Level	Applied Voltage (A)	Electrolyte Concentration (B)	IEG(C)
1	**0.6524**	**0.7203**	**0.6451**
2	0.5308	0.5572	0.5531
3	0.5835	0.4892	0.5685
Delta	0.1216	0.2311	0.0919
Rank	2	1	3

where, y_i is normalized value, x_i is measured response value, 'min' and 'max' represents the minimum and maximum value of x_i and *i is* a number of response sequences.

Once the normalization of the sequence is done, the next step is to determine the grey relational coefficients (GRC) by using Eq. 13. 'β' is the identification coefficient whose value varies from 0 to 1. In this study, equal weightage is given to each parameter i.e., β is taken as 0.5 which is most commonly used in GRA. Table 10 shows the normalized and GRCs of the response parameters.

$$\text{GRC} = \epsilon_i(k) = \frac{\Delta_{min} + \beta\Delta_{max}}{\Delta_i + \beta\Delta_{max}} \tag{13}$$

Where, Δ_i is the difference between the maximum and sequential response parameters, Δ_{min} *and* Δ_{max} are the minimum and maximum value ofΔ_i.

GRG is assessed by considering an average of GRC values as given in Eq. 14.

$$\text{GRG} = (\gamma\mathbf{i}) = \frac{\mathbf{1}}{\boldsymbol{n}}\sum_{k=1}^{n}\epsilon_i(k) \tag{14}$$

Table 10 shows the calculated GRGs along with their ranks for the experimental results while Fig. 17 shows the relationship between them. GRG with higher-order suggests that the experimental results corresponding to that grade are closer to

Table 12 ANOVA results for GRG

Parameters	DOF	Sum of Squares	Variance	F-Value	Percentage Contribution (%)
Applied Voltage	2	0.0223	0.0111	9.71	18.01
Electrolyte Concentration	2	0.0846	0.0423	36.84	68.34
IEG	2	0.0146	0.0072	6.33	11.79
Error	2	0.0023	0.0011		1.86
Total	8	0.1238			

Table 13 Confirmation Results for GRG

Response Parameters	Initial conditions (A1, B2, C3)	Optimum levels (A1, B1, C1)	
		Predicted	Experimental
GRG	0.5605	0.8400	0.8226
Improvement in GRG	0.2621		

achieve the ideal response parameters [64]. Thus, a combination of optimum parameters based on the analysis of GRG is given as A1B1C1 (35 V-15 wt.% -25 mm) (Fig. 17). It is corresponding to experiment number 1.

However, it is very much required to analyze the effect of each control parameter on the GRGs by taking all three levels into consideration. Therefore, GRG means are used to obtain the final combination of input process parameters as shown in Fig. 18. The GRG means are also given in Table 11.

Based on delta ranking, the optimum combination for the combined response parameters i.e. High MRR, low HAZ, low HT, low ROC, and low CE are computed as A1B1C1 (35 V, 15%, 25 mm) (Fig. 18). Results indicate that electrolyte concentration is the most dominant parameter for controlling the response parameters followed by the applied voltage and then the IEG. A low value of electrolyte concentration minimizes the electrical conductivity, thereby, decreases the spark intensity. Hence, it reduces HAZ, HT, ROC, and CE. A lower value of applied voltage also produces better results in terms of HAZ, HT, ROC, and CE alongside compromised MRR. The low applied voltage causes less electrochemical reactions and mitigates the spark intensities over the work material. Hence, less heat conduction into the work material and also, reduced side spark.

5.2 ANOVA

ANOVA is implemented to identify the percentage of contributions of process parameters that influence the multi-response parameters. Table 12 highlights the ANOVA results of GRG. Results indicate that electrolyte concentration is the most presiding input parameter with a percentage contribution of 68.34% followed by applied voltage (18.01%) and then the IEG (11.79%). This observation is found to agree with the rank obtained in mean GRG for input process parameters as given in Table 11.

6 Confirmation Tests

A confirmation test is important to perform for validating the enrichment of the response parameters at the optimum level. The GRG is predicted by using Eq. 15.

$$\overline{\gamma} = \gamma \mathrm{m} + \sum_{i=1}^{k} \left(\overline{\gamma} k - \gamma \mathrm{m} \right) \tag{15}$$

where, $\overline{\gamma}$ is the predicted GRG, γ_m is the total mean GRG, $\overline{\gamma}_k$ is the mean GRG at the optimum level of parameters and k is the number of parameters. The total mean GRG is 0.5889.

At optimum levels of input process parameters (A1, B1, and C1), the estimated GRG is computed as 0.8400. Table 13 illustrates the results of the confirmation test which has been carried out at the optimum levels. An average of the three tests has been considered for validating the results. It has been seen that the results obtained from the confirmation tests are in strong agreement with the predicted results of the GRGs. Figure 19 shows the comparison of micro-holes machined at initial machining condition (A1B2C3) and optimum machining condition (A1B1C1). Figure 20a-c shows the micro-holes machined at the initial machining condition while Fig. 20d-f

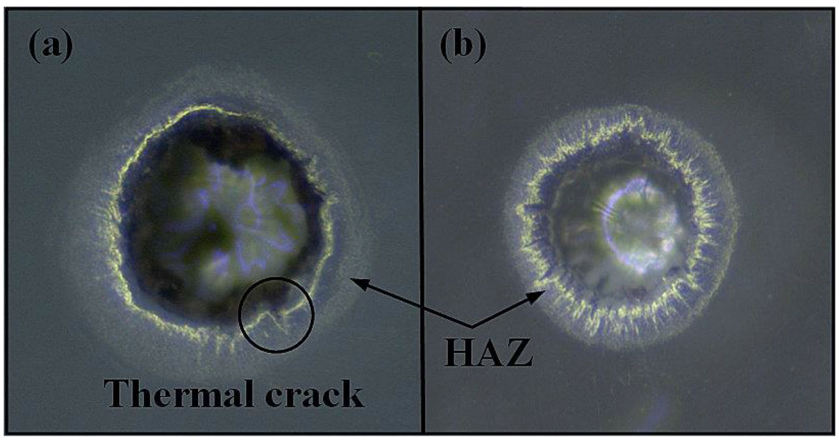

Fig. 19 Micro-hole drilled at **a** initial machining condition (A1B2C3) **b** optimum machining condition (A1B1C1)

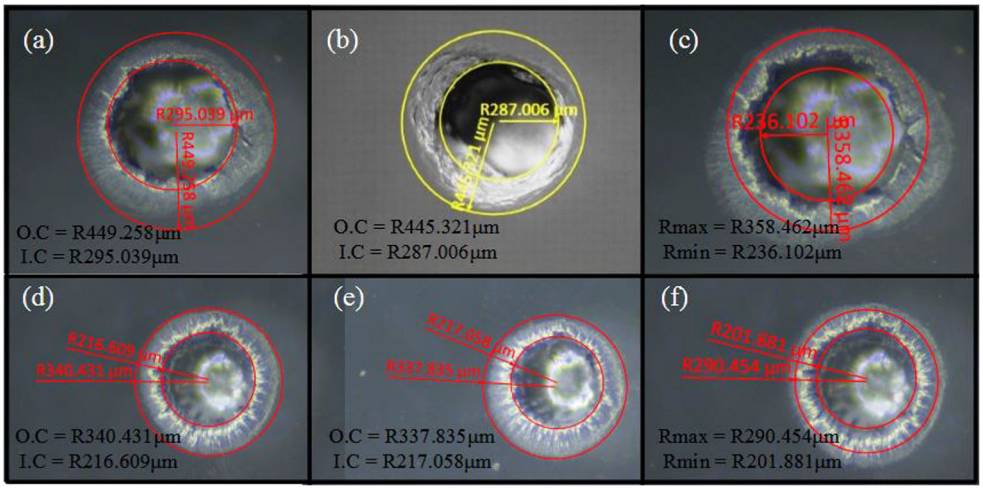

Fig. 20 Micro-holes drilled at **a-c** initial machining condition, A1B2C3 **d-f** optimum machining condition, A1B1C1; OC is outer circle radius, IC is inner circle radius

shows the micro-holes machined at optimum machining conditions. It is depicted from the figure that HAZ and ROC decrease from an initial condition to an optimum condition as hole entrance diameter decreases (Fig. 20a-b and d-e). There is a decrease in CE due to a decrease in the difference between R_{max} and R_{min} (Fig. 20c and f). Fig. 21 shows the cross-sectional microscopic image of the drilled micro-holes. An improvement in taperness is clearly seen in micro-hole drilled at optimum machining condition (A1B1C1, Fig. 21b) from initial machining condition (A1B2C3, Fig. 21a).

Confirmatory results indicate that there is an improvement in HAZ from 0.3209 mm^2 to 0.2124 mm^2, improvement in HT from 0.1986 to 0.1741, improvement in ROC from 0.0881 mm to 0.0143 mm, improvement in CE from 0.1165 mm to 0.0781 mm. MRR is compromised at 0.5285 mm^3/min. An improvement of 0.2621 is observed in the GRG from an initial condition (A1B2C3) to optimum conditions (A1B1C1). A higher GRG value represents the condition of obtaining the desired results as it is closer to the ideally normalized value [60]. GRG at initial and experimental conditions is 0.5605 and 0.8226 (Table 13). This improvement is seen in terms of an increase in GRG at the experimental condition which is closer to the higher GRG value (Table 10). Thus, multiple response characteristics are improved in this study during silica (Quartz) micro-drilling operation.

It has been found that no explicit data has been provided by the researchers on micro-hole quality in terms of HAZ, HT, ROC, and CE simultaneously during silica micro-hole drilling operation. Figure 22 compares the trend of present study results with the previously reported studies [17, 37, 65–67]. It is noticed that the trend of the measured responses is found similar in all the cases. However, some differences in the response values are observed and accounted for due to the different machining conditions such as the utilization of constant tool feed method, rotational tool and pulse voltage to machine the silica material.

The GRA based multi-response optimized results in this study reported a significant improvement in MRR when compared with the results of Goud et al. [37] and Jain et al. [38]. A decrease in HAZ, ROC, and CE is also noticed when compared to Chen et al. [32], Jain et al. [38], and Wang et al. [68] respectively (Table 14). The difference in the result is majorly due to (i) different machining conditions such as applied voltage, electrolyte concentration, tool feed, and tool rotation and (ii) different methods of drilling i.e., tool feed mechanism.

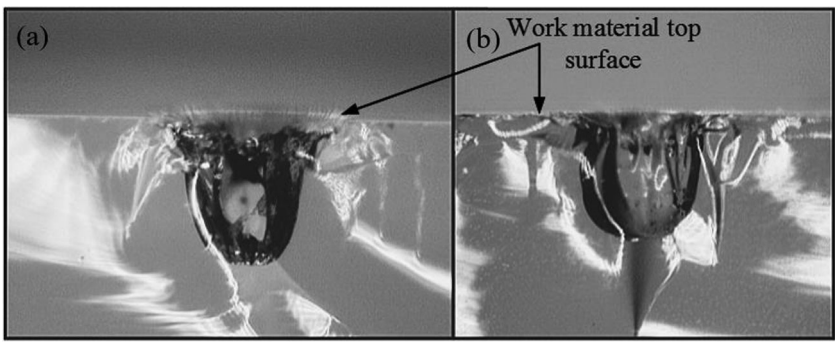

Fig. 21 A cross-sectional view of micro-holes drilled at **a** initial machining condition (A1B2C3) **b** optimum machining condition (A1B1C1)

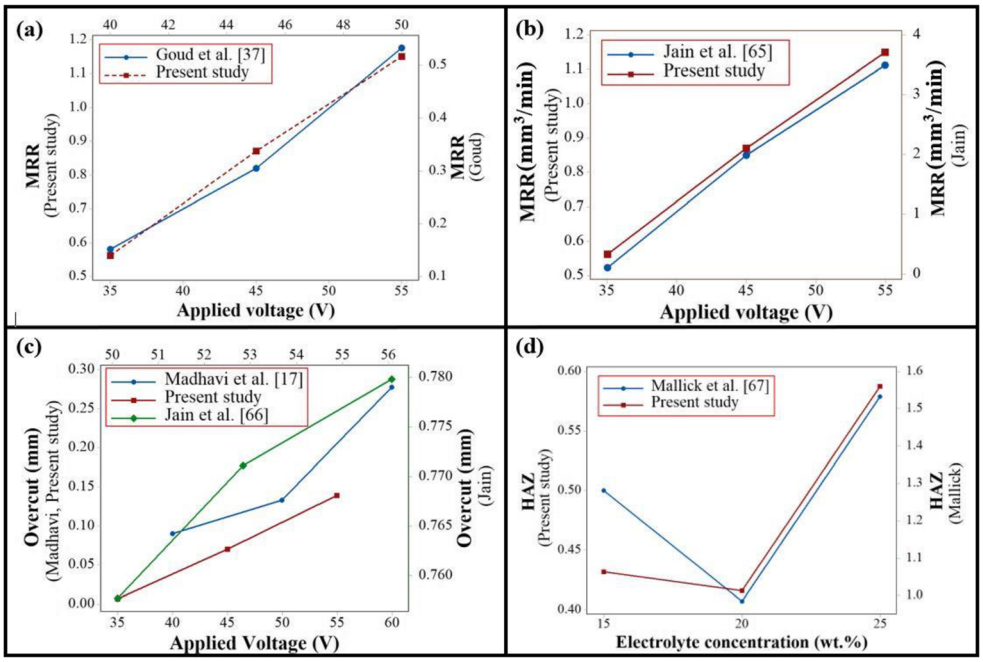

Fig. 22 Comparison of responses with previously reported work **a-b** MRR at different voltages, 20 wt% NaOH, **c** Overcut at different voltages, 20 wt.% NaOH, **d** HAZ at different NaOH concentrations, 35 V

7 Conclusions

In this present investigation, the performance evaluation of the ECDM process was performed on MRR, HAZ, HT, ROC, and CE during micro-drilling of silica (quartz) work material. The machining performance is analyzed with the application of the S/N ratio and GRA for deducing the optimum range of process parameters. The advantage of utilizing GRA over S/N ratio has been emphasized by converting the multi-objective optimization into single-objective optimization. The fusion of MRR (maximizing) and HAZ, HT, ROC, and CE (minimizing) has been done to obtain parametric optimization for all the responses simultaneously. The major conclusions drawn from the study are given underneath:

- Single response optimization suggests that applied voltage is the main dominating parameter for MRR and ROC while electrolyte concentration is the dominating parameter for HAZ, HT, and CE. All responses increase with the increase in applied voltage and electrolyte concentration.
- The combination of parameters for multi-response optimization using GRA is determined as an applied voltage at 35 V, electrolyte concentration at 15 wt.%, and the IEG at 25 mm.
- ANOVA results show that the contribution order for multi-response optimization is electrolyte concentration, applied voltage, and IEG. Thus, electrolyte concentration is the most presiding parameter with a contribution of 68.34% for controlling all the responses.
- This methodology is suitable for performing multi-response optimization and can be applied to establish a combination of process parameters for improving the ECDM performance while machining silica work material.

Table 14 Comparison of responses observed in the present study and other reported studies

Ref.	Response Parameters					GRG improvement
	MRR (mm^3/min)	HAZ (mm^2)	HT (radian)	ROC (mm)	CE (mm)	
Present study	0.5285	0.2124 mm^2	0.1741	0.0143	0.0781	0.2621
Goud et al. [37]	0.4166	–	–	0.0515	–	0.0949
Jain et al. [38]	0.1294*	–	–	0.1080	–	–
Chen et al. [32]	–	1.732 mm^2	–	–	–	–
Wang et al. [68]	–	–	–	–	0.244	–

MRR Material removal rate, *HAZ* Heat-affected zone, *HT* Hole Tapering, *ROC* Radial overcut, *CE* Circularity error, *GRG* Grey relational grade

*Computed from the results available in the reported work

References

1. Sandison ME, Zagnoni M, Abu-hantash M, Morgan H (2007) Micromachined glass apertures for artificial lipid bilayer formation in a microfluidic system. J Micromech Microeng 17:S189–S196. https://doi.org/10.1088/0960-1317/17/7/S17
2. San H, Zhang H, Zhang Q, YuY CX (2013) Silicon – glass-based single piezoresistive pressure sensors for harsh environment. J Micromech Microeng 23:075020. https://doi.org/10.1088/0960-1317/23/7/075020
3. Isabella O, Moll F, Krč J, Zeman M (2010) Modulated surface textures using zinc-oxide films for solar cells applications. Phys Status Solidi Appl Mater Sci 207:642–646. https://doi.org/10.1002/pssa.200982828
4. Bruckenstein S, Shay M (1985) Experimental aspects of use of the quartz crystal microbalance in solution. Electrochim Acta 30:1295–1300
5. Rattan N, Mulik RS (2018) Experimental set up to improve machining performance of silicon dioxide (quartz) in magnetic field assisted TW-ECSM process. Silicon 10(6):2783–2791. https://doi.org/10.1007/s12633-018-9818-z
6. Feng H, Xiang D, Wu B, Zhao B (2019) Ultrasonic vibration-assisted grinding of blind holes and internal threads in cemented carbides. Int J Adv Manuf Technol 104(1–4):1357–1367. https://doi.org/10.1007/s00170-019-04024-2
7. Belyaev A, Polupan O, Dallas W, Ostapenko S, Hess D, Wohlgemuth J (2006) Crack detection and analyses using resonance ultrasonic vibrations in full-size crystalline silicon wafers. Appl Phys Lett 88(11):111907
8. Tang Y, Fuh JYH, Loh HT, Wong YS, Lim YK (2008) Laser dicing of silicon wafer. Surf Rev Lett 15(01n02):153–159
9. Wuthrich R, Fascio V (2005) Machining of non-conducting materials using electrochemical discharge phenomenon-an overview. Int J Mach Tools Manuf 45:1095–1108
10. Basak I, Ghosh A (1997) A Mechanism of material removal in electrochemical discharge machining a theoretical model and experimental verification. J Mater Process Technol 71:350–359. https://doi.org/10.1016/S0924-0136(97)00097-6
11. Basak I, Ghosh A (2003) A Mechanism of spark generation during electrochemical discharge machining a theoretical model and experimental verification. J Mater Process Technol 62:46–53. https://doi.org/10.1016/0924-0136(95)02202-3
12. Kulkarni A, Sharan R, Lal GK (2002) An experimental study of discharge mechanism in electrochemical discharge machining. Int J Mach Tools Manuf 42:1121–1127. https://doi.org/10.1016/S0890-6955(02)00058-5
13. Sarkar BR, Doloi B, Bhattacharyya B (2006) Parametric analysis on electrochemical discharge machining of silicon nitride ceramics. Int J Adv Manuf Technol 28(9–10):873–881. https://doi.org/10.1007/s00170-004-2448-1
14. Wüthrich R, Hof LA, Lal A, Fujisaki K, Bleuler H, Mandin P, Picard G (2005) Physical principles and miniaturization of spark assisted chemical engraving (SACE). J Micromech Microeng 15(10):S268–S275
15. Wuthrich R, Hof LA (2005) The gas film in spark assisted chemical engraving SACE—a key element for micro-machining applications. Int J Mach Tools Manuf 46:828–835. https://doi.org/10.1016/jijmachtools200507029
16. Fascio V, Wuthrich R, Bleuler H (2004) Spark assisted chemical engraving in the light of electrochemistry. Electrochim Acta 49:3997–4003. https://doi.org/10.1016/j.electacta.2003.12.062
17. Bindu MJ, Hiremath SS (2019) Machining and characterization of channels and textures on quartz glass using μ-ECDM process. Silicon, pp 1-13. https://doi.org/10.1007/s12633-019-0083-6
18. Oza AD, Kumar A, Badheka V et al (2019) Traveling wire electrochemical discharge machining (TW-ECDM) of quartz using zinc coated Brass wire: investigations on material removal rate and kerf width characteristics. Silicon, pp 1-12. https://doi.org/10.1007/s12633-019-0070-y
19. Singh M, Singh S, Kumar S (2019) Experimental investigation for generation of micro-holes on silicon wafer using electrochemical discharge machining process. Silicon, pp 1-7. https://doi.org/10.1007/s12633-019-00273-8
20. Antil P (2019) Experimental analysis on wear behavior of PMCs reinforced with electroless coated silicon carbide particulates. Silicon 11(4):1791–1800. https://doi.org/10.1007/s12633-018-9995-9
21. Zhang Y, Xu Z, Zhu Y, Zhu D (2016) Machining of a film-cooling hole in a single-crystal super alloy by high-speed electrochemical discharge drilling. Chin J Aeronaut 29(2):560–570
22. Liu JW, Yue TM, Guo ZN (2010) An analysis of the discharge mechanism in electrochemical discharge machining of particulate reinforced metal matrix composites. Int J Mach Tools Manuf 50(1):86–96. https://doi.org/10.1016/j.ijmachtools.2009.09.004
23. Jain VK, Tandon S, Kumar PK (1990) Experimental investigations into electrochemical spark machining of composites. J Eng Ind 112(2):194–197. https://doi.org/10.1115/1.2899567
24. McGeough JA, Khairy ABM, Munro W (1983) Theoretical and experimental investigation of the relative effects of spark erosion and electrochemical dissolution in electrochemical arc machining. Ann CIRP 32:1113–1116. https://doi.org/10.1016/S0007-8506(07)63373-3
25. Kurafuji H, Suda K (1968) Electrical discharge drilling of glass. Ann CIRP 16:415–419
26. Sundaram M, Chen YJ, Rajurkar K (2019) Pulse electrochemical discharge machining of glass-fiber epoxy reinforced composite. CIRP Ann 68(1):169–172. https://doi.org/10.1016/jcirp201904113
27. Tang W, Kang X, Zhao W (2019) Experimental investigation of gas evolution in electrochemical discharge machining process. Int J Electrochem Sci 14:970–984
28. Bhuyan BK, Yadava V (2014) Modelling and optimization of travelling wire electro-chemical spark machining process. Int J Indus Sys Eng 18(2):139–158. https://doi.org/10.1504/IJISE.2014.064703
29. Malik A, Manna A (2016) An experimental investigation on developed WECSM during micro slicing of e-glass fibre epoxy composite. Int J Adv Manuf Technol 85:2097–2106. https://doi.org/10.1007/s00170-016-8858-z
30. Bhattacharyya B, Doloi BN, Sorkhel SK (1999) Experimental investigations into electrochemical discharge machining (ECDM) of non-conductive ceramic materials. J Mater Process Technol 95:145–154. https://doi.org/10.1016/S0924-0136(99)00318-0
31. Crichton IM, McGeough JA (1985) Studies of the discharge mechanisms in electrochemical arc machining. J Appl Electrochem 15:113–119. https://doi.org/10.1007/BF00617748
32. Chen JC, Lin YA, Kuo CL, Ho CC, Yau WH (2019) An improvement in the quality of holes drilled in quartz Glassby electrochemical discharge machining. Smart Sci 7(3):169–174. https://doi.org/10.1080/23080477.2019.1597579
33. Saranya S, Sankar AR (2018) Fabrication of precise micro-holes on quartz substrates with improved aspect ratio using a constant velocity-feed drilling technique of an ECDM process. J Micromech Microeng 28(12):125009. https://doi.org/10.1088/1361-6439/aae8f5
34. Tang W, Kang X, Zhao W (2017) Enhancement of electrochemical discharge machining accuracy and surface integrity using side-insulated tool electrode with diamond coating. J Micromech Microeng 27(6):065013. https://doi.org/10.1088/1361-6439/aa6e94
35. Saranya S, Ravi Sankar A (2017) Fabrication of precise microchannels using a side-insulated tool in a spark assisted chemical engraving process. Mater Manuf Process 33:1422–1428. https://doi.org/10.1080/10426914.2017.1401728

36. Han MS, Min BK, Lee SJ (2008) Modeling gas film formation in electrochemical discharge machining processes using a side-insulated electrode. J Micromech Microeng 18(4):045019
37. Goud MM, Sharma AK (2017) On performance studies during micromachining of quartz glass using electrochemical discharge machining. J Mech Sci Technol 31:1365–1372. https://doi.org/10.1007/s12206-017-0236
38. Jain VK, Adhikary S (2008) On the mechanism of material removal in electrochemical spark machining of quartz under different polarity conditions. J Mater Process Technol 200:460–470. https://doi.org/10.1016/j.jmatprotec.2007.08.071
39. Elhami S, Razfar MR (2017) Effect of ultrasonic vibration on the single discharge of electrochemical discharge machining. Mater Manuf Process 33(4):1–8. https://doi.org/10.1080/10426914201713281 13
40. Daneshmand S, Monfared V, Lotfi Neyestanak AA (2017) Effect of tool rotational and Al_2O_3 powder in electro discharge machining characteristics of NiTi-60 shape memory alloy. Silicon 9(2):273–283. https://doi.org/10.1007/s12633-016-9412-1
41. Liu JW, Yue TM, Guo ZN (2013) Grinding-aided electrochemical discharge machining of particulate reinforced metal matrix composites. Int J Adv Manuf Technol 68(9–12):2349–2357. https://doi.org/10.1007/s00170-013-4846-8
42. Liu J, Lin Z, Yue T, Guo Z, Jiang S (2018) An analysis of the tool electrode working mechanism of grinding-aided electrochemical discharge machining of MMCs. Int J Adv Manuf Technol 99(5–8):1369–1378. https://doi.org/10.1007/s00170-018-2591-8
43. Kuo KY, Wu KL, Yang CK, Yan BH (2015) Effect of adding SiC powder on surface quality of quartz glass microslit machined by WECDM. Int J Adv Manuf Technol 78:73–83
44. Yadav P, Yadava V, Narayan A (2019) Experimental investigation for performance study of wire electrochemical spark cutting of silica epoxy Nanocomposites. Silicon, pp 1-11. https://doi.org/10.1007/s12633-019-00197-3
45. Rattan N, Mulik RS (2017) Experimental investigations and multi-response optimization of silicon dioxide (quartz) machining in magnetic field assisted TW-ECSM process. Silicon 9(5):663–673. https://doi.org/10.1007/s12633-018-9818-z
46. Liu Y, Zhang C, Li S, Guo C, Wei Z (2019) Experimental study of micro electrochemical discharge machining of ultra-clear glass with a rotating helical tool. Processes 7:19.5
47. Rajput V, Goud M, Suri NM (2019) Study on effective process parameters: towards the better comprehension of ECDM process. Int J Mod Manufact Technol 11(2):105–118
48. Kavimani V, Prakash KS, Thankachan T, et al. (2019) WEDM parameter optimization for Silicon@r-GO/Magneisum composite using Taguchi based GRA coupled PCA. Silicon, pp 1–15. https://doi.org/10.1007/s12633-019-00205-6
49. Muthuramalingam T, Vasanth S, Vinothkumar P, Geethapriyan T, Rabik MM (2019) Multi criteria decision making of abrasive flow oriented process parameters in abrasive water jet machining using Taguchi–DEAR methodology. Silicon 10(5):2015–2021. https://doi.org/10.1007/s12633-017-9715-x
50. Antil P, Singh S, Singh P (2018) Taguchi's methodology based parametric analysis of material removal rate during ECDM of PMCs. Procedia Manuf 26:469–473
51. Julong D (1989) Introduction to Grey system theory. J Grey Syst 1:1–24
52. Antil P (2019) Modelling and multi-objective optimization during ECDM of silicon carbide reinforced epoxy composites. Silicon, pp 1–14. https://doi.org/10.1007/s12633-019-00122-8
53. Kumar JS, Kalaichevlan K (2018) Taguchi-Grey multi-response optimization on structural parameters of honeycomb Core Sandwich structure for low velocity impact test. Silicon 10(3):879–889
54. Kumar PN, Rajadurai A, Muthuramalingam T (2018) Multi-response optimization on mechanical properties of silica Fly ash filled polyester composites using Taguchi-Grey relational analysis. Silicon 10(4):1723–1729
55. Ziki AJD, Didar TF, Wuthrich R (2012) Micro-texturing channel surfaces on glass with spark assisted chemical engraving. Int J Mach Tools Manuf 57:66–72. https://doi.org/10.1016/j.ijmachtools.2012.01.012
56. Goud MM, Sharma AK, Jawalkar CS (2016) A review on material removal mechanism in electrochemical discharge machining ECDM and possibilities to enhance the material removal rate. Precis Eng 45:1–17. https://doi.org/10.1016/j.precisioneng.2016.01.007
57. Rajput V, Goud M, Suri N M (2019) Performance analysis on the effect of different electrolytes during glass micro drilling operation using ECDM. I-Manag J Futur Eng Technol 14(4): 5–13. https://doi.org/10.26634/jfet.14.4.15788
58. Sarikaya M, Gullu A (2014) Multi-response optimization of MQL parameters using Taguchi based GRA in turning of difficult to cut alloy Haynes 25. J Clean Prod 1-11. https://doi.org/10.1016/j.jclepro.2014.12.020
59. Mian S H, Umer U, Alkhalefah H (2019) Optimization of scanning parameters in coordinate metrology using grey relational analysis and fuzzy logic. Math Probl Eng. https://doi.org/10.1155/2019/2085962
60. Maillard P, Despont B, Bleuler H, Wuthrich R (2007) Geometrical characterization of micro-holes drilled in glass by gravity-feed with spark assisted chemical engraving (SACE). J Micromech Microeng 17(7):1343–1349
61. Abdullah AB, Sapuan SM, Samad Z (2015) Roundness error evaluation of cold based on profile measurement technique. Int J Adv Manuf Technol 80:293–300. https://doi.org/10.1007/s00170-015-6961-1
62. Tang L, Yang S (2013) Experimental investigation on the electrochemical machining of 00Cr12Ni9Mo4Cu2 material and multi-objective parameters optimization. Int J Adv Manuf Technol 67:2909–2916
63. Sindhu D, Thakur L, Chandna P (2019) Multi-objective optimization of rotary ultrasonic machining parameters for quartz glass using Taguchi-Grey relational analysis (GRA). Silicon 11(4):2033–2044. https://doi.org/10.1007/s12633-018-0019-6
64. Antil P, Singh S, Manna A (2018) Electrochemical discharge drilling of SiC reinforced polymer matrix composite using Taguchi's Grey relational analysis. Arab J Sci Eng 43:1257–1266. https://doi.org/10.1007/s13369-017-2822-6
65. Jain VK, Chak SK (2000) Electrochemical spark trepanning of alumina and quartz. Mach Sci Technol 4(2):277–290. https://doi.org/10.1080/10940340008945710
66. Jain VK, Priyadarshni D (2013) Fabrication of micro-channels in ceramics (quartz) using electrochemical spark micro machining (ECSM). Proc of global engineering, Science and Technology conference, Singapore
67. Mallick B, Sabah Hameed A, Sarkar BR, Doloi B, Bhattacharyya B (2020) Experimental investigation for improvement of micro-machining performances of μ-ECDM process. Materials Today: Proceedings
68. Wang J, Jia Z, Guo YB (2018) Shape-cutting of quartz glass by spark discharge-assisted diamond wire sawing. J Manuf Process 34:131–139. https://doi.org/10.1016/j.jmapro.2018.06.001